Monthly Notices
of the
ROYAL ASTRONOMICAL SOCIETY

MNRAS **461,** 3457–3482 (2016)
Advance Access publication 2016 June 24

doi:10.1093/mnras/stw1525

Galaxies in the EAGLE hydrodynamical simulation and in the Durham and Munich semi-analytical models

Quan Guo,[1,2]★ Violeta Gonzalez-Perez,[3,2]★ Qi Guo,[4] Matthieu Schaller,[2] Michelle Furlong,[2] Richard G. Bower,[2] Shaun Cole,[2] Robert A. Crain,[5]† Carlos S. Frenk,[2] John C. Helly,[2] Cedric G. Lacey,[2] Claudia del P. Lagos,[6,7] Peter Mitchell,[2] Joop Schaye[8] and Tom Theuns[2]

[1]*Leibniz-Institut für Astrophysik Potsdam, An der Sternwarte 16, D-14482 Potsdam, Germany*
[2]*Institute for Computational Cosmology, Department of Physics, University of Durham, South Road, Durham DH1 3LE, UK*
[3]*Institute of Cosmology and Gravitation, University of Portsmouth, Dennis Sciama Building, Portsmouth PO1 3FX, UK*
[4]*Key Laboratory for Computational Astrophysics, The Partner Group of Max Planck Institute for Astrophysics, National Astronomical Observatories, Chinese Academy of Sciences, Beijing 100012, China*
[5]*Astrophysics Research Institute, Liverpool John Moores University, 146 Brownlow Hill, Liverpool L3 5RF, UK*
[6]*International Centre for Radio Astronomy Research, University of Western Australia, 35 Stirling Highway, Crawley, WA 6009, Australia*
[7]*Australian Research Council Centre of Excellence for All-sky Astrophysics (CAASTRO), 44 Rosehill Street Redfern, NSW 2016, Australia*
[8]*Leiden Observatory, Leiden University, PO Box 9513, NL-2300 RA Leiden, the Netherlands*

Accepted 2016 June 22. Received 2016 May 27; in original form 2015 November 27

ABSTRACT

We compare global predictions from the EAGLE hydrodynamical simulation, and two semi-analytic (SA) models of galaxy formation, L-GALAXIES and GALFORM. All three models include the key physical processes for the formation and evolution of galaxies and their parameters are calibrated against a small number of observables at $z \approx 0$. The two SA models have been applied to merger trees constructed from the EAGLE dark matter only simulation. We find that at $z \leq 2$, both the galaxy stellar mass functions for stellar masses $M_* < 10^{10.5}\,\mathrm{M}_\odot$ and the median specific star formation rates (sSFRs) in the three models agree to better than 0.4 dex. The evolution of the sSFR predicted by the three models closely follows the mass assembly history of dark matter haloes. In both EAGLE and L-GALAXIES there are more central passive galaxies with $M_* < 10^{9.5}\,\mathrm{M}_\odot$ than in GALFORM. This difference is related to galaxies that have entered and then left a larger halo and which are treated as satellites in GALFORM. In the range $0 < z < 1$, the slope of the evolution of the star formation rate density in EAGLE is a factor of $\approx$1.5 steeper than for the two SA models. The median sizes for galaxies with $M_* > 10^{9.5}\,\mathrm{M}_\odot$ differ in some instances by an order of magnitude, while the stellar mass–size relation in EAGLE is a factor of $\approx$2 tighter than for the two SA models. Our results suggest the need for a revision of how SA models treat the effect of baryonic self-gravity on the underlying dark matter. The treatment of gas flows in the models needs to be revised based on detailed comparison with observations to understand in particular the evolution of the stellar mass–metallicity relation.

Key words: methods: analytical – methods: numerical – galaxies: evolution – galaxies: formation – cosmology: theory.

1 INTRODUCTION

The formation and evolution of galaxies in a cosmological context involves a multitude of physical processes, such as stellar and active galactic nuclei (AGN) feedback, that are hard to constrain directly by observations (e.g. Somerville & Davé 2015). Many of these poorly constrained processes are pivotal for addressing fundamental questions concerning the growth of structure in the Universe.

In the current paradigm, the ΛCDM cosmological model, galaxies are formed in the potential wells generated by the gravity of the underlying dark matter distribution (e.g. White & Rees 1978; Blumenthal et al. 1986; White & Frenk 1991), which is assumed to evolve through gravitational interactions (Peebles 1980; Davis et al. 1985). There have been two main approaches to understanding the

★ E-mail: guotsuan@gmail.com (QG); violegp@gmail.com (VG-P)
† Royal Society University Research Fellow.

formation and evolution of galaxies: semi-analytical (SA) models and hydrodynamical simulations.

The fundamental difference between the two approaches is that hydrodynamical simulations simultaneously solve the equations of gravity and hydrodynamics for dark matter, gas and stars (recent examples include Oppenheimer et al. 2010; Puchwein & Springel 2013; Dubois et al. 2014; Okamoto, Shimizu & Yoshida 2014; Vogelsberger et al. 2014; Khandai et al. 2015; Steinborn et al. 2015), while SA models follow the evolution of the gas partitioned by the dark matter halo it occupies (recent examples include Guo et al. 2013; Gonzalez-Perez et al. 2014; Lee et al. 2014; Lu et al. 2014; Henriques et al. 2015; Lacey et al. 2015; Ruiz et al. 2015). Dark matter haloes are defined as ≈200 times overdense dark matter structures that are gravitationally bound. The evolution of dark matter haloes can be described by merger trees, which are hierarchical structures recording the haloes mass growth and merger history over cosmic time. The halo merger trees needed by SA models are generated from either *N*-body dark matter simulations or using Monte Carlo techniques (e.g. Parkinson, Cole & Helly 2008).

Another important difference between the two methods is that, while in hydrodynamical simulations no a priori assumptions need to be made about the properties of galaxies, in SA models, baryons are divided into discrete components: gas halo, gas disc, stellar disc, gas bulge, stellar bulge. Each component has idealized spatial, thermal and velocity profiles. SA models work by integrating differential equations that describe how mass, energy, angular momentum and metals are exchanged between these different components. These equations encapsulate the physical processes that are thought to be the most relevant for the formation and evolution of galaxies (see Baugh 2006; Benson 2010, for reviews of SA models).

Both SA models and hydrodynamical simulations require subgrid prescriptions. SA models use physical models dependent on global galaxy properties, for example in supernova (SN) feedback the wind speed can depend on the disc circular velocity. Hydrodynamical simulations attempt to model the physical processes in more detail than SA models, since in these simulations the gas and star particles are followed explicitly. For example, the radiative cooling rate in hydrodynamical simulations is, in principle, determined by atomic physics (as it is in SA models). Nevertheless, subgrid models on the scale of the interstellar medium (ISM) structure, are necessary to account for the limited numerical resolution and physics in hydrodynamical simulations. Moreover, in both hydrodynamical simulations and SA models, most subgrid models are a mixture of physical and empirical ingredients which require calibration.

Hydrodynamical simulations and SA models are complementary, with their own advantages and disadvantages. The first capture the complexity of gas and stellar dynamics in a way that SA models cannot, which is invaluable when studying, for example, the details of gas accretion on to galaxies. They are, however, limited by the extraordinary computational cost of having to resolve very small scales over cosmological volumes. Therefore, the simulated volumes have been modest (e.g. Genel et al. 2012; Zolotov et al. 2012; Hopkins et al. 2014; Marinacci, Pakmor & Springel 2014), although hydrodynamical simulations of cosmological volumes have started to become available (Dubois et al. 2014; Hirschmann et al. 2014a; Khandai et al. 2015), and multiscale approaches are needed to account for processes that cannot be directly resolved (e.g. Vogelsberger et al. 2014; Crain et al. 2015). SA models, on the other hand, are more flexible and require a relatively modest computational cost. Thus, these models can be run over large cosmological volumes and can also be used to explore extensively the parameter space in a statistically significant way employing techniques such as Monte Carlo Markov chains (e.g. Henriques et al. 2009; Lu et al. 2011b; Benson 2014), particle swarm (Ruiz et al. 2015) and emulator techniques (Bower et al. 2010). Although the flexibility of SA models is achieved at the cost of approximations that might be more inaccurate than those introduced in hydrodynamical simulation, these models predict global galactic properties that are qualitatively similar (e.g. De Lucia et al. 2010; Fontanot et al. 2011; Lu et al. 2014; Knebe et al. 2015).

Previous comparisons between hydrodynamical simulations and SA models have focused on either comparing a handful of objects (e.g. Stringer et al. 2010; Hirschmann et al. 2012) or on a single aspect of the physics, for example gas cooling (Benson et al. 2001; Yoshida et al. 2002; Helly et al. 2003; Benson & Bower 2011; Lu et al. 2011a). In some of the latter cases, stripped-down versions of SA models are used, in which all the other physical processes relevant for galaxy formation apart from that under scrutiny are switched off (e.g. Cattaneo et al. 2007; Saro et al. 2010; Neistein et al. 2012; Monaco et al. 2014). In the case of gas cooling studies, this usually implies turning off star formation and thus ignoring the gas flowing back into the halo due to feedback. Thus, such studies are limited and thus it is important to also compare complete and realistic models of galaxy formation and evolution as those presented here.

Recently, the first cosmological hydrodynamical simulations that reproduce some of the fundamental observations of the local galaxy population have been published (e.g. Vogelsberger et al. 2014; Schaye et al. 2015). This has been achieved by modelling and calibrating the subgrid physical processes that shape the gas cooling, the star and black hole (BH) formation, the metal enrichment and the stellar and AGN feedback. Furthermore, the parameters of the subgrid models have been constrained by comparing the hydrodynamical simulation results against observations, in a similar way as has traditionally been done for SA models. The new hydrodynamical simulations have been run in cosmological volumes, although these remain a factor up to ≈400 smaller than that used for the Millennium simulation (Springel 2005), which is the basis of several SA models (e.g. Bower et al. 2006; De Lucia & Blaizot 2007).

Given these recent advances in hydrodynamical simulations and the overlap in physical processes modelled, it is now an appropriate time to examine thoroughly the similarities and differences of galaxy samples produced by different complete galaxy formation models. This comparison will allow us to explore the impact of variations in the subgrid implementation across the models. Such a comparison will not only help in exploring better parametrizations of subgrid physics, but it will lay the foundations for comparing galaxies in greater detail on smaller scales, where the advantages of hydrodynamical simulations are most important.

Recently, Somerville & Davé (2015) compared results from published hydrodynamical simulations and SA models, finding remarkable agreement between the global properties of model galaxies, such as the galaxy stellar mass function (GSMF) and the stellar mass–star formation rate (SFR) relations. In this work we expand on that study, by comparing a hydrodynamical simulation with two SA models built upon merger trees extracted from dark matter only realizations of the same initial conditions as the hydrodynamical simulation.

EAGLE is one of the first cosmological hydrodynamical simulation to model galaxy populations whose basic properties are broadly consistent with observations (Crain et al. 2015; Furlong et al. 2015a,b; Lagos et al. 2015b; Schaye et al. 2015; Trayford et al. 2015). This level of agreement with observations has been achieved by calibrating the free parameters of the subgrid physics modelling to match

the observed local GSMF and stellar mass–size relations. A similar level of agreement with observations was previously only achieved by SA models and ad hoc empirical models constructed with that specific purpose (e.g. Favole et al. 2015). In this paper, we make the first detailed comparison between the results from this state-of-the-art cosmological hydrodynamical simulation and two SA models, GALFORM and L-GALAXIES.

In order to make a fair comparison, while focusing on the modelling of the physical processes relevant for galaxy evolution, we have generated dark matter merger trees from the EAGLE dark matter-only (EAGLEDMO) simulation, populating the haloes with galaxies using SA models. Some small changes have been introduced in the GALFORM model in order to use the same initial mass function (IMF) as in EAGLE and L-GALAXIES, and also to obtain a similar level of agreement with the observed passive fraction of galaxies at $z = 0$. The model parameters in L-GALAXIES and GALFORM are separately calibrated against observations according to their own criteria, namely the $z = 0$ GSMF and luminosity functions, respectively (see Section 2.2.3 for details). The models are therefore *not* explicitly calibrated to match each other.

Based on the output galaxy catalogues, we compare the predictions of several global properties of model galaxies. In this work, we are interested in exploring the similarities and differences in the model galaxy population with the aim of probing the physics included in the model. The three models used in this paper describe the same set of key physical processes, thought to be relevant to galaxy formation and evolution; however, the details of the implementation can be quite different among the models. Thus, it is interesting to compare global galactic properties from different modelling approaches in order to understand the origin of the largest discrepancies. This work is also meant as the foundation for a future comparison between individual objects (Mitchell et al., in preparation). The aim of this paper is to determine the similarities and differences between the three models and understand the physical origin of the latter. This work does not aim to establish which model performs better compared to a certain set of observable. Thus, we include only very limited observational data just as a reference. Moreover, no attempt is made in this work to discuss how the models compare with the presented observations as this will detract the text from our main purpose. Detailed comparisons of EAGLE, L-GALAXIES and GALFORM with observations can be found in other studies (Guo et al. 2011; Gonzalez-Perez et al. 2014; Furlong et al. 2015a,b; Henriques et al. 2015; Lacey et al. 2015; Lagos et al. 2015b; Schaye et al. 2015).

The remainder of this paper is organized as follows. In Section 2, we briefly introduce the EAGLE simulation and the two SA models, GALFORM and L-GALAXIES. In Section 3 we compare the GSMFs, the stellar mass–halo mass relations for central galaxies and the halo occupation distributions of the models. The star-forming sequence is defined in Section 5, where properties of galaxies separated into star-forming and passive populations are explored. The mass–metallicity and mass–size relations are discussed in Sections 6 and 7, respectively. The appendix contains a discussion on the definition of the halo masses in the models. The conclusions of this work are presented in Section 8.

2 MODELS OF GALAXY FORMATION

For this work, we compare global galaxy properties predicted by the hydrodynamical simulation EAGLE and two different SA models of galaxy formation, GALFORM and L-GALAXIES, built on the halo merger trees from the EAGLEDMOsimulation. The EAGLEDMO and main EAGLE simulations model the same volume, with initial conditions produced using the same phases except that the volume of EAGLEDMO is sampled with 1504^3 dark matter particles, while EAGLE is sampled with 1504^3 dark matter and 1504^3 baryonic particles. The properties of the simulations are summarized in Table 1. The simulations assume the ΛCDM best-fitting cosmological parameters from the Planck Collaboration XVI (2014) data given in Table 2. The initial conditions were generated using second-order Lagrangian perturbation theory with the method of Jenkins (2010) and evolve from $z = 127$.

Table 1. Parameters characterizing both the EAGLEDMO and main EAGLE simulations. From top-to-bottom the rows show: comoving box size; number of dark matter particles (there is initially an equal number of baryonic particles); initial gas particle mass for the main EAGLE simulation; dark matter particle mass for the EAGLEDMO and the EAGLE simulations; comoving gravitational softening length; maximum physical softening length.

Property	EAGLEDMO, EAGLE
L (comoving Mpc)	100
N	1504^3
m_g	–, 1.81×10^6 M$_\odot$
m_{dm}	1.15×10^7 M$_\odot$, 9.70×10^6 M$_\odot$
ϵ (comoving kpc), $z > 2.8$	2.66
ϵ (proper kpc), $z < 2.8$	0.70

Table 2. The cosmological parameters used from table 9 in Planck Collaboration XVI (2014): Ω_m, Ω_Λ and Ω_b are the average densities of matter, dark energy and baryonic matter in units of the critical density at redshift zero, H_0 is the Hubble parameter, σ_8 is the square root of the linear variance of the matter distribution when smoothed with a top-hat filter of radius $8\,h^{-1}$Mpc.

Ω_m	0.307
Ω_Λ	0.693
Ω_b	0.048 25
$h \equiv H_0/(100$ km s^{-1} Mpc$^{-1})$	0.6777
σ_8	0.8288

Below we summarize the characteristics of EAGLE, GALFORM and L-GALAXIES. At the end of this section, we have also included a description of the limits in stellar mass used in this paper for both the whole galaxy population and those separated into star-forming and passive galaxies. It is important to note again that the most fundamental difference between hydrodynamical simulations and SA models is that the former tracks simultaneously the evolution of dark matter, gas and stellar particles, while the latter follows the evolution of baryons in haloes in an idealized way.

2.1 EAGLE

The EAGLE simulation suite comprises a set of runs with different box sizes and mass resolutions. Many of its derived properties are now publicly available (McAlpine et al. 2016). Here we show results from the largest EAGLE simulation (introduced by Schaye et al. 2015). The simulation was performed with a version of the GADGET code (last described by Springel 2005), modified by using a state-of-the-art formulation of smoothed particle hydrodynamics (SPH), ANARCHY (Dalla Vecchia, in preparation; Schaller et al. 2015b), and subgrid models for galaxy formation.

Haloes in the EAGLE simulation were identified using the Friends-of-Friends (FoF) algorithm (Davis et al. 1985) and self-bound

Table 3. The observational data used to calibrate the three default models used in this work.

Model	Observational data used in the model calibration
EAGLE	GSMF at $z \approx 0.1$ from GAMA (Baldry et al. 2012) and SDSS (Li & White 2009), the stellar mass–size relation at $z \approx 0.1$ (Shen et al. 2003; Baldry et al. 2012) and the $z \approx 0$ $M_{\rm BH}$–M_* relation (McConnell & Ma 2013).
GALFORM	b_J-band (Norberg et al. 2002) and K-band (Driver et al. 2012) luminosity functions at $z \approx 0$, the passive fraction at $z \approx 0$ (Gilbank et al. 2011; Bauer et al. 2013) and the $M_{\rm BH}$–$M_{\rm Bulge}$ relation (Häring & Rix 2004).
L-GALAXIES	GSMF at $z \approx 0$ (Baldry et al. 2008; Li & White 2009) and the $M_{\rm BH}$–$M_{\rm Bulge}$ relation (Häring & Rix 2004).

structures within the haloes were then identified using the SUBFIND code (Springel et al. 2001; Dolag et al. 2009). In EAGLE, the galaxies are defined as the baryonic component of the gravitationally bound subhaloes. Below, we briefly describe the main aspects of the subgrid physics and some of the definitions relevant here.

2.1.1 Subgrid physics

Star formation. Star formation is implemented following the method of Schaye & Dalla Vecchia (2008). The SFR per unit mass of particles is computed using an analytical prescription designed to reproduce the observed Kennicutt (1998) relation in disc galaxies (Schaye & Dalla Vecchia 2008). Gas particles are converted into star particles stochastically. The threshold in hydrogen density required to form stars is metallicity dependent, with lower metallicity gas having a higher threshold. Thus, trying to capture the metallicity dependence of the phase transition from warm atomic to cold molecular gas (Schaye 2004).

Metal enrichment and gas cooling. The simulations assume a Chabrier (2003) stellar IMF in the range 0.1–100 $\rm M_\odot$, with each individual star particle representing a single stellar population. The star particles release metals into the ISM gradually over their lifetime through three evolutionary channels: Type Ia SNe, winds and SNe from massive stars, and AGB stars using the method introduced by Wiersma et al. (2009b). The yields for each process are taken from Portinari, Chiosi & Bressan (1998), Marigo (2001) and Thielemann et al. (2003). The 11 elements that dominate the cooling curve are tracked individually as proposed by Wiersma, Schaye & Smith (2009a). Assuming that the gas is in ionization equilibrium, these elements are used to compute the cooling and photoheating rates of the gas in the presence of the cosmic microwave background and the X-ray and UV backgrounds from galaxies and quasars given by the model of Haardt & Madau (2001).

Feedback from star formation and AGNs. Over the course of its lifetime, a simple stellar population will inject energy into the ISM. In EAGLE, this energy is multiplied by an efficiency factor that depends on the local gas metallicity and density (Crain et al. 2015). The energy from the stars is transferred to the surrounding gas in the form of heat. The temperature of the surrounding gas is raised instantly by $10^{7.5}$ K. This is implemented stochastically on one or more gas particles in the neighbourhood of the star (Dalla Vecchia & Schaye 2012). This gas, once heated, remains coupled in a hydrodynamic sense with its SPH neighbours in the ISM, and therefore exerts a form of feedback locally that can directly affect radiative cooling and star formation. Galactic winds develop without imposing a predefined mass-loading or direction and without disabling radiative cooling.

Supermassive BH seeds with mass $10^5\,h^{-1}\,\rm M_\odot$ are injected in haloes above $10^{10}\,h^{-1}\,\rm M_\odot$ (Springel 2005) and grow through mergers and accretion of low angular momentum gas (Rosas-Guevara et al. 2015; Schaye et al. 2015). AGN feedback depends on the mass accreted by the BH and is modelled by the injection of thermal energy into the gas surrounding the BH such that its temperature is raised by $\Delta T = 10^{8.5}$ K (Booth & Schaye 2009; Dalla Vecchia & Schaye 2012).

2.1.2 Aperture measurements

The stellar mass of a galaxy in the EAGLE simulation is defined to be the sum of the masses of all the stellar particles that are bound to the corresponding subhalo within a 3D aperture of radius 30 proper kiloparsec (Schaye et al. 2015). The stellar mass computed in this way is found to be similar to the mass computed within Petrosian apertures from the simulation at $z = 0.1$. Meanwhile, in SA models, the stellar mass is accumulated with time, starting from the initial seed of hot gas in a halo and taking into account the fraction of mass returned to the ISM by SNe and stellar winds for a simple stellar population and in the case of L-GALAXIES the losses due to tidal disruption.

For consistency with the galaxy mass definition, SFRs of galaxies in EAGLE are measured within spherical apertures of 30 proper kpc. As the majority of the star formation occurs close to the centres of galaxies, this aperture has a negligible effect on the total SFR recovered.

2.1.3 Calibration of the parameters

As discussed by Schaye et al. (2015), the free parameters controlling the subgrid model for feedback were chosen in order to reproduce the stellar mass functions at $z \approx 0$ from the GAMA survey by Baldry et al. (2012) and from the SDSS survey by Li & White (2009), the galaxy mass–size relation as reported by Shen et al. (2003) and Baldry et al. (2012) and the relation between the mass of the central supermassive BH and the total stellar mass of galaxies derived from observations compiled by McConnell & Ma (2013, see also Table 3).

2.2 Semi-analytical models

SA models use simplified, partly phenomenological recipes and rules to follow the fate of baryons in a dark-matter-dominated universe in which structure grows hierarchically through gravitational instability (see Baugh 2006; Benson 2010, for an overview of SA models).

GALFORM (Cole et al. 2000; Bower et al. 2006; Gonzalez-Perez et al. 2014; Lacey et al. 2015) and L-GALAXIES (Springel 2005; Croton

et al. 2006; Guo et al. 2011; Henriques et al. 2015), the two models used for this study, follow the physical processes that shape the formation and evolution of galaxies, including:

(i) the collapse and merging of dark matter haloes;
(ii) the shock-heating and radiative cooling of gas inside dark matter haloes, leading to the formation of galaxy discs;
(iii) star formation bursts that can be triggered either by mergers or disc instabilities;
(iv) the growth of supermassive BHs in galaxies;
(v) feedback from SNe, from AGN and from photoionization of the intergalactic medium;
(vi) chemical enrichment of stars and gas, assuming the instantaneous recycling approximation (as opposed to EAGLE, where a non-instantaneous recycling is implemented);
(vii) galaxy mergers driven by dynamical friction within common dark matter haloes, leading to the formation of stellar spheroids, which can also be produced by disc instabilities.

The models also compute the sizes of the disc and bulge components of galaxies. The end product of the calculation is a prediction for the abundances and properties of galaxies that reside within dark matter haloes of different characteristics.

In order to make a fair comparison with EAGLE, the two SA models which we use here have been adapted from the published models described by Guo et al. (2013) and Gonzalez-Perez et al. (2014). Specifically, the SA models have been run on merger trees extracted from the EAGLEDMO simulation, assuming the same Planck cosmology (Planck Collaboration XVI 2014, table 9) as adopted by EAGLE. Both the underlying simulation and the cosmology are different from the *WMAP7* cosmology used by Guo et al. (2013) and Gonzalez-Perez et al. (2014), and thus, a recalibration of their free parameters was required in order to satisfactorily reproduce the corresponding set of observational data summarized in Section 2.2.3. Moreover, EAGLE assumes a Chabrier IMF (Chabrier 2003), which is the default in Guo et al. (2013) but not in the published Gonzalez-Perez et al. (2014) model. Thus, there is a corresponding change in the metal yield and recycled fractions in the SA models (see B for further details). For both EAGLE and L-GALAXIES, galaxy photometry has been derived using the stellar population synthesis (SPS) models of Bruzual & Charlot (2003). In the case of GALFORM, the models of Conroy, White & Gunn (2010) are used, which include a very similar library of stellar spectra to Bruzual & Charlot (2003) and also account for the contribution of thermally pulsating asymptotic giant branch stars (see Gonzalez-Perez et al. 2014; Trayford et al. 2015, for a comparison of different SPS models).

The most significant difference between the published GALFORM model and that presented here by default, is the inclusion of gradual ram-pressure stripping of hot gas in the satellite galaxies of the GALFORM model, as opposed to the instantaneous stripping assumed by Gonzalez-Perez et al. (2014, see Section 2.2.2). This was included to ensure all three models provided a reasonable match to the observed passive fractions at $z = 0$. Note that the Gonzalez-Perez et al. (2014) model has previously been used including such an update of the hot gas stripping, in the context of studying early-type galaxies (Lagos et al. 2014). Throughout this study, we comment on the extent of the effect of stripping the hot gas instantaneously or gradually, for results that are significantly affected by this choice.

An overview of the GALFORM and L-GALAXIES models is provided below, focused on the aspects where they differ.

2.2.1 *Halo finder and merger trees*

Both SA models are based on merger trees extracted from the same EAGLEDMO simulation; however, there are differences in the methods applied to construct them. GALFORM is based on subhalo merger trees built with the Dhalo algorithm (Jiang et al. 2014), while L-GALAXIES subhalo merger trees are constructed following Springel (2005), De Lucia & Blaizot (2007) and Boylan-Kolchin et al. (2009). As in EAGLE, both methods use the FoF algorithm to identify haloes, but ensuring that haloes artificially linked by this algorithm are treated as separate objects. SUBFIND is used to identify the self-bound substructure in haloes. Initial SUBFIND merger trees are built by tracking particles between snapshots. Both methods can identify the descendants of a halo at any of the following two snapshots in the case of L-GALAXIES and five in the DHALO algorithm. This feature was implemented in order to improve the identification of substructure in close encounters that can be mistaken for real mergers. In effect, the only conceptual difference between the two methods is that the DHALO algorithm enforces a monotonic growth of halo mass.

In Appendix A, we show the halo mass functions from the three models considered, focusing on variations that arise from the different definitions of halo mass. Although systematic discrepancies do exist due to these definitions, the dominant difference is between the EAGLE and the EAGLEDMO simulations, due to the impact that early expulsion of baryons has on the subsequent growth of dark matter haloes (e.g. Sawala et al. 2013; Velliscig et al. 2014; Schaller et al. 2015a).

Central and satellite galaxies. For GALFORM, host haloes are defined either at the final output of the simulation or just before a halo merges with another more massive one. The centre of the most massive subhalo is defined as the halo centre. The DHALO algorithm determines the main progenitor of this subhalo as the one that contributed the most bound part of the descendant. This process is carried out starting at the final output time and working backwards towards high redshift. This results in the assignment of one central subhalo to every halo in such a way that the same subhalo is considered to be the central as long as the halo exists (see appendix A of Jiang et al. 2014).

In L-GALAXIES, as in EAGLE, central galaxies are those hosted by the most massive subhalo (main subhalo) which usually has most of the mass of its FoF group. This choice for defining the main branch, tries to reduce the chance of the centre swapping to a different subhalo between snapshots (McAlpine et al. 2016).

In GALFORM, satellite galaxies remain as such until either they merge with the central galaxy in their host halo or the end of the simulation is reached. This is not the case in L-GALAXIES, in which satellite galaxies can be reclassified as centrals if they are far enough from the virial radius of the halo that was hosting them.

2.2.2 *Physics*

Star formation. In GALFORM, the cold gas corresponds to the ISM gas, including the molecular, atomic and ionized phases. In this model, the quiescent star formation in galaxy discs explicitly depends on the molecular component of the gas (Lagos et al. 2011). This empirically motivated calculation assumes that during quiescent star formation, the surface density of the SFR is proportional to the surface density of molecular hydrogen in the ISM (Blitz & Rosolowsky 2006; Bigiel et al. 2008; Leroy et al. 2008). The SFR from starbursts in GALFORM is assumed to be simply proportional to

the total mass of cold gas present in galaxy bulges and inversely proportional to a star formation time-scale (Granato et al. 2000).

In L-GALAXIES, stars are assumed to form from the gas in the quiescent mode. The cold gas disc and stellar disc in the model are distinct, and both can grow continuously in mass and angular momentum in a physically plausible way (Guo et al. 2013, section 3.3). Stars form in a cold gas disc according to a simplified empirical Kennicutt relation (Kennicutt 1998), but only in regions where the surface gas density exceeds a critical value. This critical value is related to the gas velocity dispersion and the rotation curve of the galaxy. This star-formation threshold reflects that the star formation is expected to be possible only in dense enough regions (Kauffmann 1996). The SFR from starbursts in L-GALAXIES is assumed to be proportional to the total mass of cold gas and the mass ratio of two merger progenitors whenever merger happens.

Stellar feedback. When massive stars die, they inject large amounts of energy into the ISM in SN explosions. In both GALFORM and L-GALAXIES, this can cause ejection of gas from galaxies and haloes, but the details are different. In both models, cold gas is ejected from galaxies at a rate proportional to the SFR, with the proportionality factor (called the mass-loading factor) depending on the circular velocity. In GALFORM this dependence is a simple power law, while in L-GALAXIES it has a more complicated form, but in both models, the mass-loading factor decreases with increasing circular velocity. Furthermore, in GALFORM the circular velocity used is that at the disc half-mass radius for disc star formation, and at the bulge half-mass radius for starbursts, while in L-GALAXIES it is the peak circular velocity of the subhalo. In GALFORM, cold gas is ejected directly from the galaxy out of the halo. In L-GALAXIES, there is instead a two-stage ejection process: cold gas is ejected into the halo, and SN also inject energy into the halo, with an efficiency that also depends on circular velocity; hot gas is then ejected from the halo in a quantity depending on the available energy, with an explicit constraint that the energy used cannot exceed the total SN energy.

In both models, gas that has been expelled from the halo is added to a reservoir outside the halo, from where it gradually returns to the hot halo, being reincorporated at the halo virial temperature. In GALFORM the return time-scale is simply proportional to the halo dynamical time, while in L-GALAXIES it also depends on the halo circular velocity, with the return time-scale decreasing with increasing circular velocity.

AGN feedback. The onset, by AGN activity, of the suppression of the gas cooling in haloes is assumed to occur in both L-GALAXIES and GALFORM only for haloes hosting galaxies whose central BH is growing in mass through gas accretion.

In GALFORM, the quasi-hydrostatic cooling is assumed to occur in haloes hosting galaxies such that $t_{\rm cool} > t_{\rm ff}/\alpha_{\rm cool}$, where $t_{\rm cool}$ is the cooling time of the gas, $t_{\rm ff}$ is the free-fall time for the gas to reach the centre of the halo and $\alpha_{\rm cool}$ is a model parameter, set to $\alpha_{\rm cool} = 0.52$. $\alpha_{\rm cool}$ is set to 0.6 in both the published version (Gonzalez-Perez et al. 2014) and the version with an instantaneous stripping of hot gas in satellite galaxies shown in this study. When a halo is undergoing quasi-hydrostatic cooling, the gas cooling is suppressed if the luminosity released by gas accreted on to a central supermassive BH balances or exceeds the cooling luminosity (see Bower et al. 2006; Fanidakis et al. 2011, for further details).

In L-GALAXIES, it is assumed that the hot-mode accretion of mass on to the BH deposits energy with a 10 per cent efficiency, heating up the halo hot gas. The BH accretion rate in this model is assumed to be a function of the ratio of hot gas mass to subhalo DM mass, the virial velocity of the halo and the mass of the central BH. The efficiency of the growth of BHs due to such hot-mode accretion is a model parameter. BHs can also grow by mergers (see Croton et al. 2006; Guo et al. 2011, for further details).

Sizes. For the calculation of disc sizes, both SA models assume conservation of specific angular momentum and centrifugal equilibrium. The sizes of spheroids are estimated in both models assuming virial equilibrium and energy conservation. To determine disc sizes, L-GALAXIES follows the full angular momentum vectors of haloes and discs, and separates the contribution from stars and gas in the disc (Guo et al. 2011, section 3.3), while GALFORM only tracks the magnitudes of the disc and halo angular momentum, assuming that the disc and halo angular momentum are always aligned (Cole et al. 2000, section 4.4 and appendix C). In both models, the disc angular momentum is determined by the halo formation and gas cooling history. In GALFORM, this is then used to obtain both the disc radius and the circular velocity at the disc half-mass radius by solving self-consistently the combined gravity of the disc, spheroid and halo (Cole et al. 2000). In L-GALAXIES, the circular velocity of the disc is assumed to be equal to the maximum circular velocity of the host halo (Guo et al. 2011).

GALFORM includes the self-gravity of discs and spheroids when computing disc sizes, while L-GALAXIES ignores this, which is a significant assumption, in particular for massive galaxies whose inner regions are, in principle, not dominated by dark matter. Furthermore, GALFORM also models the contraction of the dark matter halo due to the gravity of the baryonic component. We note that if the baryonic self-gravity was turned off in GALFORM then the circular velocity used by this model would be close to the maximum halo circular velocity, as assumed by L-GALAXIES, because in that case, GALFORM would use the uncontracted dark matter halo value of the circular velocity at the half-mass radius of the disc.

Although the gravity of the baryons should be taken into account when calculating the distribution of dark matter in a halo, the simplified model for halo contraction adopted by GALFORM appears to overestimate the effect of the baryons compared to gas dynamical simulations (e.g. Gnedin et al. 2004), this maybe because the adiabatic invariance assumed in the contraction model is violated by the short time-scale of SN driven outflows in low mass haloes (Sawala et al. 2013; Newman, Ellis & Treu 2015).

Environmental processes. In both L-GALAXIES and GALFORM, environmental effects, such as ram-pressure stripping of gas, are implemented in a way that only impacts the evolution of satellite galaxies. Note that these environmental effects are naturally included in hydrodynamical simulations such as EAGLE. The SA models used in this work assume a gradual ram-pressure stripping of the hot gas in satellite galaxies. L-GALAXIES also includes a basic model of tidal stripping. In this model, the hot gas in a subhalo is distributed following the underlying dark matter and it is affected in the same way as the dark matter by tidal stripping. Once a subhalo has been entirely disrupted, the remaining galaxy will be disrupted when the baryon density within its half-mass radius is smaller than the main halo density at the pericentre of the subhalo orbit. The components of the disrupted satellite galaxy are then assigned to a population of intracluster stars (Guo et al. 2011).

Many of the GALFORM published models, including Gonzalez-Perez et al. (2014), adopt instantaneous ram-pressure stripping, as opposed to gradual stripping, of the hot gas in satellite galaxies (but see Lagos et al. 2014, 2015a). Here we use the parametrization for

the gradual stripping of hot gas in satellites introduced by Font et al. (2008) following the analysis of the hydrodynamical simulations of cluster environments by McCarthy et al. (2008). Assuming instantaneous stripping results in the exhaustion of most of the satellite galaxy gas reservoirs, quickly quenching their star formation, as no further supply of gas is accreted. Thus, most satellites in models with instantaneous stripping are passively evolving. The assumptions made about the gas in satellite galaxies affect the results related to separating galaxies into star-forming and passive subsets. However, the change in the ram-pressure stripping model has only a small effect on other results, such as the calibration diagnostics (see Section 2.2.3).

Although there is plenty of observational evidence indicating the importance of gas stripping for galaxies within dense environments (e.g. Scott et al. 2013; Boselli et al. 2014; Fumagalli et al. 2014), the modelling of this process is unclear. One of the primary uncertainties is related to the fate of the stripped gas once it has been ejected from the subhalo by stellar feedback. Another concern is that, as observations are limited to cluster environments and to ram-pressure stripping of the ISM (and not the ram-pressure stripping of hot gas), galaxies in lower density environments in SA models might be overquenching the star formation (Hirschmann et al. 2014b; McGee, Bower & Balogh 2014). We will investigate the role of ram-pressure stripping through the comparison with EAGLE and between the GALFORM models with instantaneous and gradual stripping. In the subsequent discussion, we comment on the instantaneous stripping GALFORM model when significant differences arise relative to the default GALFORM model.

2.2.3 *Calibration*

For GALFORM, the Gonzalez-Perez et al. (2014) model was calibrated to reproduce the b_J and K-band luminosity functions at $z = 0$ from Norberg et al. (2002) and Driver et al. (2012) and the BH–bulge stellar mass ($M_{\rm BH}$–$M_{\rm Bulge}$) relation from Häring & Rix (2004), see also Table 3. As mentioned earlier, here we are using a modified version of this model, for which we have adopted the Planck cosmology, the Conroy et al. (2010) SPS model and a Chabrier IMF, as opposed to the previously used Kennicutt IMF, with the corresponding values for the yield and recycled fraction. These modifications did not significantly alter the $z = 0$ luminosity functions used for calibrating the free parameters in the model. As mentioned, the instantaneous stripping of hot gas in satellite galaxies is replaced with a gradual stripping model. The predicted passive fraction for the model with gradual stripping is closer to that observed (Gilbank et al. 2011; Bauer et al. 2013). The change in the b_J- and K-band luminosity functions at $z = 0$ resulting from assuming gradual stripping is large enough to require a slight lowering of the threshold for the AGN feedback to be effective and recover the same level of agreement with the observed luminosity functions. The individual impact of each of these variations is discussed in detail in Gonzalez-Perez et al. (in preparation).

The published Guo et al. (2013) model was calibrated primarily to reproduce the $z \approx 0$ stellar mass function observed by Baldry, Glazebrook & Driver (2008) and Li & White (2009) and the $M_{\rm BH}$–$M_{\rm Bulge}$ relation of Häring & Rix (2004), as is summarized in Table 3. During the calibration of this model a further condition ensured that the cold gas fractions increase with decreasing stellar mass, as observations suggest. The L-GALAXIES model used in this work has been recalibrated such that it still reproduces the aforementioned observations by slightly modifying the stellar and AGN feedback in order to account for the change in cosmology, halo mass resolution and time sampling of the merger trees, that arise as a result of the model being built on the EAGLEDMO simulation.

2.3 Stellar mass limits and star-forming galaxies

In order to reduce the sampling effects associated with the limited resolution of the EAGLE simulation, only galaxies with a minimum stellar mass $M_* \gtrsim 10^8\,{\rm M}_\odot$ are considered. We impose this cut in stellar mass in the three models. Moreover, in the EAGLE simulations, galaxies with low SFRs can present quantized behaviour in the sense that an SN explosion in a single stellar particle can modify the star formation by a significant amount, due to poor sampling. Thus, a minimum number of about 30 star-forming particles is needed in order for the SFR to be reliable, based on resolution tests from Schaye et al. (2015) at low and Furlong et al. (2015b) at high redshifts. This limit is shown by the sloping magenta lines in Fig. 7.

In this work, we separate passive from star-forming galaxies based on their specific star formation rate (sSFR=SFR/M_*). The chosen boundaries are highlighted in Fig. 7 (horizontal dashed magenta): $\log_{10}({\rm sSFR/Gyr^{-1}}) = -2, -1.04, -0.97$ at redshifts $z = 0, 1, 2$, respectively. Galaxies above these cuts are considered to be star-forming and galaxies below are considered as passive. Furlong et al. (2015b) set these limits, which correspond to $\approx$1 dex below the mean sSFR from a compilation of observed star-forming galaxies. We have tried different values of the sSFR cut used to split galaxies into star-forming and passive populations, including those from Franx et al. (2008). Although some of the results are quantitatively affected by the exact value of this cut, such as the passive fractions, the discussion and conclusions in this paper are insensitive the particular value chosen, within 1σ of the values stated above.

Note that the sSFR value chosen as a boundary for separating galaxies into passive and star-forming intersects with that corresponding to the minimum of 30 star-forming particles at a stellar mass that decreases with increasing redshift. Thus, the minimum stellar mass for measuring SFRs in EAGLE varies with redshift as an indirect consequence of imposing a boundary between passive and star-forming galaxies that evolves with redshift.

3 STELLAR MASSES

Many aspects of galaxy evolution are condensed into the GSMF and related quantities. In this section, we compare different stellar mass relations obtained with EAGLE, GALFORM and L-GALAXIES, for a selection of redshifts.

3.1 The galaxy stellar mass function

In Fig. 1 we show the GSMF[1] of model galaxies in EAGLE, GALFORM and L-GALAXIES at three different redshifts, $z = 0, 1, 2$. The GSMF can generally be described approximately by a Schechter function[2] (Schechter 1976), i.e. a power law and an exponential break which starts at a characteristic mass, $M_{\rm Break}$. We carry out single Schechter function fits, using the Levenberg–Marquardt algorithm through

[1] Throughout this paper, we present model distributions estimated by the standard Kernel Density Estimation with bandwidth of 0.2 (Silverman 1986) rather than histograms. This choice minimizes the dependence on the chosen starting point that simple histograms have.

[2] Other functional forms might be more appropriate than the Schechter function for describing either the mass or luminosity functions (e.g. Gunawardhana et al. 2015), in particular for cases such as the GSMF predicted by the GALFORM model, which presents a plateau just below $M_{\rm Break}$.

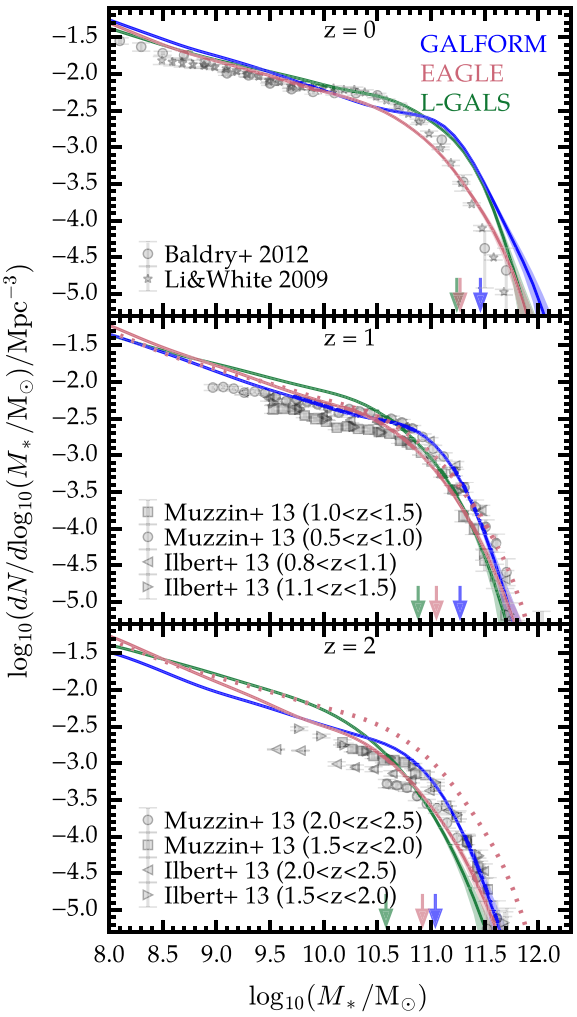

Figure 1. GSMFs in EAGLE, GALFORM and L-GALAXIES at different redshifts, as indicated by the legend, convolved with a Gaussian error of $0.07 + 0.04z$ (Behroozi, Wechsler & Conroy 2013). The shaded regions show the 1σ error from 200 bootstrap samples of galaxies taken from the whole simulation volume (note that this is a very narrow region for most stellar masses). The arrows show, in the same colour as the corresponding model, $M_{\rm Break}$ from a single Schechter function fit to the GSMFs in the range $10^8 < M_*/\,{\rm M}_\odot < 10^{12.5}$, using the 1σ errors shown. The EAGLE stellar mass function at $z = 0$ is overplotted as a red dotted line in the middle and lower panels. For reference, observational estimates of the GSMF from Li & White (2009), Baldry et al. (2012), Muzzin et al. (2013) and Ilbert et al. (2013) are included as indicated in the legend (note that when necessary, the observational data have been converted to a Chabrier IMF and the Planck cosmology). The evolution of the GSMF is remarkably similar for the three models.

least squares, to each model at all redshifts in the stellar mass range $10^8 < M_*/\,{\rm M}_\odot < 10^{12.5}$. The best-fitting parameters are given in Table 4. This provides a quantitative summary of the results shown in Fig. 1.

The GSMFs at $z = 0$ are similar for the three models. The parameters in EAGLE and L-GALAXIES were calibrated to reproduced the observed GMSF at $z = 0$, and GALFORM to reproduce the observed K-band luminosity function at $z = 0$, which follows closely the GMSF. Thus, by construction, at $z = 0$, the $M_{\rm Break}$ obtained from a single Schechter function fit to the GSMFs from the three models is similar, with a variation $\lesssim$5 per cent (see Table 4). For galaxies with

Table 4. The model GSMFs for EAGLE, GALFORM and L-GALAXIES, at three different redshifts, have been fitted to a single Schechter function, $\Phi(M) = \Phi^* {\rm e}^{-(M_*-M_{\rm Break})}(M_* - M_{\rm Break})^{1+\alpha}$, in the range $10^8 < M_*/\,{\rm M}_\odot < 10^{12.5}$ and using the 1σ errors shown in Fig. 1. For these fits, the table below presents the faint-end slope, α, the stellar mass at the knee of the GSMF, $M_{\rm Break}$, and two measures of the goodness of the fit: χ^2 and that normalized by the degrees of freedom, χ^2/ν.

EAGLE	α	$\log_{10}(M_{\rm Break}/\,{\rm M}_\odot)$	χ^2	χ^2/ν
$z = 0$	−1.43	11.2	0.047	0.0011
$z = 1$	−1.49	11.1	0.079	0.0020
$z = 2$	−1.60	10.9	0.064	0.0018
GALFORM				
$z = 0$	−1.44	11.4	0.396	0.0084
$z = 1$	−1.45	11.3	0.718	0.0167
$z = 2$	−1.47	11.0	0.421	0.0105
L-GALAXIES				
$z = 0$	−1.34	11.2	0.144	0.0036
$z = 1$	−1.35	10.9	0.012	0.0003
$z = 2$	−1.40	10.6	0.084	0.0025

$M < 10^{10.5}\,{\rm M}_\odot$, the number densities in the three models are similar, with differences $\lesssim$0.3 dex. However, in EAGLE the GSMF at the fitted $M_{\rm Break} \approx 10^{11.2}\,{\rm M}_\odot$ is a factor of ≈3 below those from the SA models. From exploring the parameter space with the SA models, it is clear that both the normalization and the position of the knee in the GSMF are mostly affected by stellar and AGN feedback (e.g. Bower, Benson & Crain 2012). Note that EAGLE was calibrated using small volumes, which do not constrain galaxies with $M_* \gtrsim M_{\rm Break}$ however the results are still consistent with observations within the (systematic) errors (Schaye et al. 2015).

The three models predict the GSMF to evolve in similar ways, such that both the overall GSMF normalization and $M_{\rm Break}$ decrease with increasing redshift. The single Schechter function fit to the GSMFs in the range $10^8 < M_*/\,{\rm M}_\odot < 10^{12.5}$, with the 1σ errors shown in Fig. 1, gives $\log_{10}(M_{\rm Break}/\,{\rm M}_\odot)$ which varies in a similar way for the three models, as indicated by the arrows in Fig. 1 (see also Table 4). For all models, the decrease in abundance is most significant for massive galaxies. The faint-end slope becomes slightly steeper with redshift in all three models (see Table 4) and this evolution is strongest for EAGLE. We have extended the comparison of model GSMFs up to $z = 4$ (not shown), finding similar trends to those reported here up to $z = 2$.

As mentioned in Section 2.2.2, the GALFORM model shown in Fig. 1 assumes that the hot gas in satellites is removed gradually as opposed to instantaneously, as assumed in the previously published model of Gonzalez-Perez et al. (2014). As we show in the next section, around $M_{\rm Break}$ the GSMF is dominated by central galaxies. These grow faster when an instantaneous ram-pressure stripping of the hot gas is assumed, at least partly because the central galaxy halo gains more gas from the satellite haloes. This has an impact on the massive end of the GSMF at $z = 0$, which is compensated for during calibration by the small change in the AGN feedback discussed in Section 2.2.3.

3.1.1 *The passive and star-forming GSMFs*

In Fig. 2 we present the GSMFs for central and satellite galaxies, separated into star-forming and passive as described in Section 2.3. Star-forming galaxies dominate the number density in the global GSMF at masses $M_* \lesssim M_{\rm Break}$, while, in the same stellar mass range, centrals dominate over satellite galaxies.

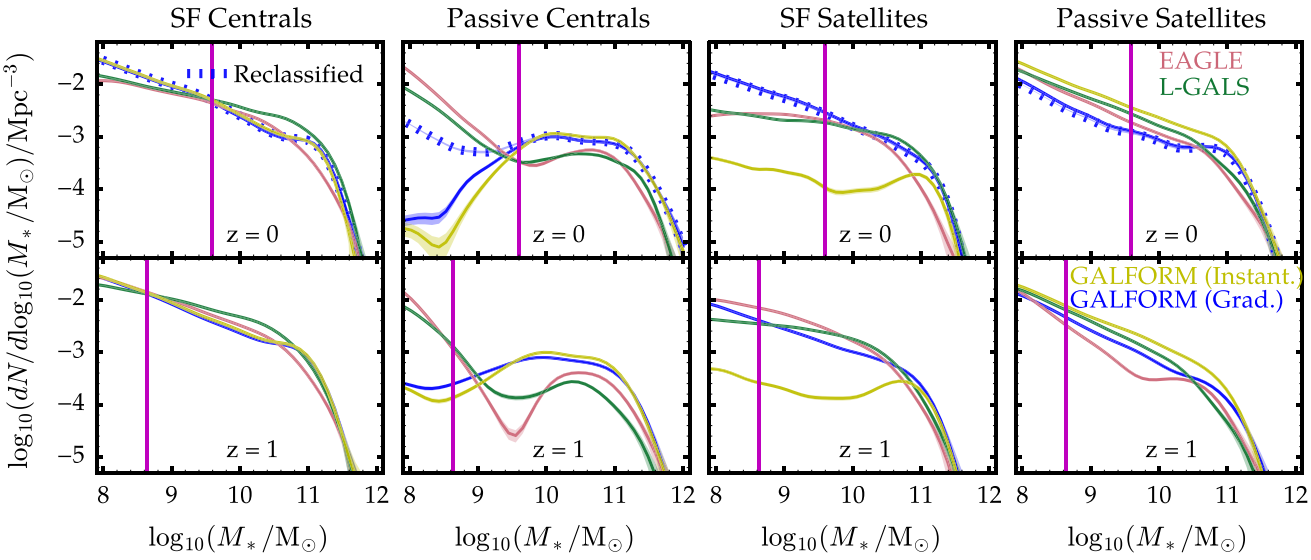

Figure 2. The GSMF at $z = 0$, top panels, and $z = 1$, bottom panels, calculated from EAGLE, GALFORM and L-GALAXIES. From left to right the columns show the GSMF of: star-forming central galaxies, passive centrals, star-forming satellite galaxies and passive satellites. The separation into star-forming and passive galaxies is described in Section 2.3. The vertical magenta lines are a guide to the resolution limits of star-forming galaxies in EAGLE. The limit evolves with redshift due to the evolving sSFR limit coupled with the need to have at least 30 star-forming particles in EAGLE to measure SFRs adequately (see Section 2.3 for further details). In this plot, we show the predictions from GALFORM assuming either gradual ('Grad.', blue lines, the default model in this paper) or instantaneous ram-pressure stripping ('Instant.', yellow lines) of the hot gas in satellite galaxies. We also show, as dotted lines, the result from reclassification as centrals of those satellite galaxies in GALFORM that are beyond one virial radius from the central galaxy of their host halo. This exercise shows that the upturn at low masses in the passive centrals GSMF for EAGLE and L-GALAXIES, shown in the second panel from the left, is at least partly due to ejected satellite galaxies, as discussed in Section 3.1.1.

The most striking difference for central galaxies seen in Fig. 2 is the upturn in the abundance at low-masses of passive centrals predicted by both EAGLE and L-GALAXIES, but not seen for galaxies in the GALFORM model. At $z = 0$, this upturn happens at $\approx 10^{9.5}$ $\mathrm{M}_\odot$, very close to the resolution limit of EAGLE for star-forming galaxies (see Section 2.3 for details). At higher redshifts, the upturn seen for EAGLE galaxies is also likely to be due to sampling, given that Furlong et al. (2015b) found the fraction of low-mass passive galaxies to vary with higher simulation resolution. In contrast, L-GALAXIES and GALFORM predictions are constrained by the halo resolution of EAGLEDMO, which mainly affects galaxies with $M_* < 10^8\,\mathrm{M}_\odot$, much lower than the mass at which the upturn starts for L-GALAXIES. In order to explore the possible origin of the upturn in the abundance of small passive centrals, we ran the GALFORM model changing in turn parameters controlling the gas cooling, star formation law (including a star formation law with an explicit threshold as described in Lagos et al. 2011) and feedback. None of these aspects were found to produce an abundance of passive central galaxies close to that from L-GALAXIES.

Further investigation revealed that the different behaviour for small masses arises from the definition of central and satellite galaxies in the models (Section 2). The most relevant difference here is that only the GALFORM model assumes that once a galaxy becomes a satellite it will remain as such until it merges with a central galaxy. In GALFORM, satellite galaxies can leave their host halo. When that happens, these galaxies experience ram-pressure stripping, even if outside their host halo. Such long-range environmental processes has been observed (e.g. Hirschmann et al. 2014b; Wetzel et al. 2014). This implies that for L-GALAXIES, galaxies that are classified as central at $z = 0$ could have undergone environmental quenching processes at earlier times. This is actually the case for around a third of the $z = 0$ centrals in the L-GALAXIES model (Hirschmann et al. 2014b; Henriques et al. 2015), which we refer to as ejected satellite galaxies (Li et al. 2013, studied the evolution the host haloes of these type of galaxies). Hence, these differences between the definition of satellite galaxies play an important role in the interpretation of results. As a test of the importance of the satellite galaxy definition at $z = 0$, we have reclassified satellite galaxies in GALFORM as centrals if they are beyond one virial radius[3] from the central galaxy of the host halo. This results in only ≈5 per cent of the satellites at $z = 0$ being reclassified. At $z = 0$, the resulting GSMFs from this reclassification are shown in Fig. 2 (dotted lines) and are found to present an upturn at $M_* \approx 10^9\,\mathrm{M}_\odot$, as expected. The effect of this reclassification exercise is negligible for galaxies that are not passive centrals.

GALFORM predicts a larger number of low-mass star-forming galaxies than the other models at $z = 0$. This suggests that either the stellar feedback in GALFORM is weaker or the reincorporation times for the gas are shorter than in the other two models; however, some other physical process might be relevant given that at higher redshift this excess is not clearly seen.

In Fig. 2 we present two flavours of the GALFORM model: the default model described in Section 2.2, which assumes a gradual stripping of the hot gas in satellite galaxies, and one assuming the stripping to be instantaneous, as used in many previous GALFORM publications (e.g. Gonzalez-Perez et al. 2014). The two right-hand panels in Fig. 2, which show satellite galaxies, reveal that the SA models assuming gradual stripping predict GSMFs are closer to those predicted by EAGLE. Instantaneous stripping results in

[3] The virial radius for this test was simply assumed to be related to the mass and circular velocity of the host halo as: $R_{\rm vir} = G \times M_{\rm host\,halo}/(V^2_{\rm host\,halo})$, with G being the gravitational constant.

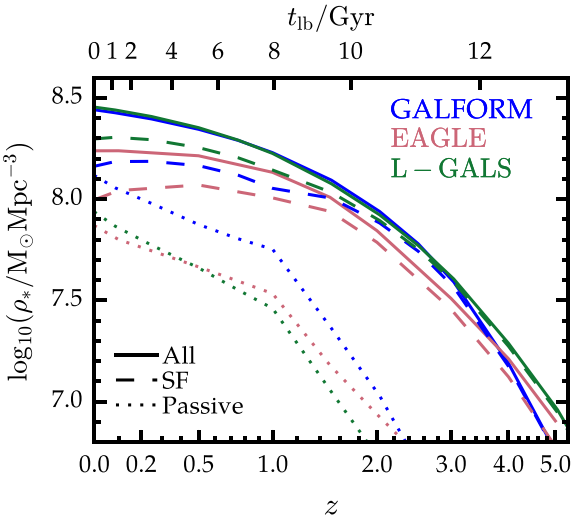

Figure 3. The stellar mass density of galaxies with $M_* > 10^8\,{\rm M}_\odot$, as a function of redshift and lookback time, $t_{\rm lb}$ Gyr, as predicted by EAGLE, GALFORM and L-GALAXIES. Solid lines show the prediction for all galaxies (note that the corresponding lines for GALFORM and L-GALAXIES are practically on top of each other), dashed lines show star-forming galaxies only and dotted lines passive galaxies only. The star-forming and passive galaxies are classified according to the boundary values of the sSFR described in Section 2.3, which are interpolated linearly in redshift. The global stellar mass density at $z < 1.5$ is dominated by galaxies with $M_* \geq 10^{10.5}\,{\rm M}_\odot$.

exhausting most of satellites gas reservoir and a quick quenching of the star formation in these galaxies, as no further supply of gas is accreted on to satellite galaxies. Thus, most satellites in the GALFORM model with instantaneous stripping are passively evolving, as can be seen in the right-hand panels of Fig. 2. The assumptions made about the gas in satellite galaxies affect the results related to the split of galaxies into star-forming and passive types.

While in the SA models the ram-pressure stripping is only modelled for the hot component in satellite galaxies, in EAGLE, as in other hydrodynamical simulations, the environment affects both cold and hot gas in all galaxies (Bahé et al. 2013). A detailed study of the differences between SA models and hydrodynamical simulations will require the comparison of individual galaxies in similar (if not the same) haloes, something that is beyond the scope of this paper.

3.2 The build-up of the stellar mass

The build-up of the GSMF is closely related to the evolution of the comoving stellar mass density, which is presented in Fig. 3 for model galaxies with stellar masses above 10^8 M$_\odot$. In turn, given that the two SA models adopt the instantaneous recycling approximation, their stellar mass density at a given redshift, $\rho_*(z_i)$, can be recovered by integrating the star formation rate comoving density (SFRD), $\dot{\rho}_*$ (shown in Fig. 6), and subtracting stellar mass losses:

$$\rho_*(z_i) = (1-R)\int_{z_i}^{z\to\infty} \dot{\rho}_*\,[(1+z)H(z)]^{-1}\,{\rm d}z. \quad (1)$$

For the SA models, $R = 0.4588$ is the fraction of mass returned to the ISM by SNe and stellar winds, which is a constant set by the adopted IMF. While in GALFORM all the stellar mass is locked in galaxies, L-GALAXIES models tidal stripping and thus a fraction of the stellar mass density is associated with the intracluster light (ICL), rather than with a particular galaxy. The exact fraction of stellar mass associated with the ICL in L-GALAXIES depends on the environment and formation histories of the galaxies involved, but we have found ≈20 per cent to be a good average approximation.

The overall build-up of the comoving stellar mass density for the two SA models, GALFORM and L-GALAXIES, is similar, as expected from the general agreement of their GSMFs at $z = 0$ and higher redshifts, seen in Fig. 1, in particular around $M_{\rm Break}$. The stellar mass density in the EAGLE model is lower than those from the two SA models: by a factor of 1.8 at $z = 0$ and a factor of 1.26 at $z = 2$. The lower stellar mass density arises from the lower normalization of the EAGLE GSMF at $M_* \sim M_{\rm Break}$ at $z = 0$, seen in Fig. 1. We have confirmed, by comparing ρ_* in different stellar mass bins, that the difference in the stellar mass density is mainly due to galaxies with $M_* \geq 10^{10.5}\,{\rm M}_\odot$, around the break of the GSMF at $z = 0$. By varying the parameters controlling different physical processes in GALFORM, we find that the stellar mass density evolution is strongly affected by the efficiency of feedback. In particular, the build-up process followed by galaxies with stellar masses around and above $M_{\rm Break}$ at $z = 0$ is strongly affected by the efficiency of AGN feedback (see also van de Voort & Schaye 2012; Crain et al. 2015).

Fig. 3 also shows the stellar mass density of star-forming galaxies (dashed lines). At $z = 0$, star-forming galaxies in both EAGLE and GALFORM contribute ≈65 per cent of the total stellar mass density, while the contribution in L-GALAXIES is ≈80 per cent. These values depend on the definition used for selecting star-forming galaxies, however, very similar results have been found when changing the boundary value by 0.3 dex. Thus, the larger fraction of star-forming galaxies might point to L-GALAXIES having less efficient AGN feedback throughout cosmic time, given that the stellar mass density is dominated by galaxies with $M_* \approx M_{\rm Break}$.

Note that a model that adopts an instantaneous stripping of the hot gas in satellites has larger numbers of passive galaxies at $z = 0$, and thus, builds its stellar mass more rapidly at $z > 1$.

3.3 The stellar mass–halo mass relation

The M_*–$M_{\rm halo}$ relation, relation can be directly related to the star formation efficiency in haloes of different masses (e.g. Behroozi et al. 2013). Converting baryons into stars can be viewed as an inefficiency process, as an illustration of this point, the stellar masses of central galaxies obtained by multiplying the host halo masses by the universal baryonic fraction is shown as a dash–dotted line in Fig. 4.

In this section, we explore the M_*–$M_{\rm halo}$ relation for *central* galaxies in EAGLE, GALFORM and L-GALAXIES, as shown in Fig. 4. $M_{\rm halo}$ is defined to be $M_{200}^{\rm crit}$, as described in the appendix. The differences between the halo mass functions of the three models are negligible relative to the differences reported below in either Figs 4 or 5. Only galaxies with stellar masses $M_* > 10^8\,{\rm M}_\odot$ are studied here (see Section 2.3).

At all redshifts, medians of the M_*–$M_{\rm halo}$ relation of the three models differ by less than 0.5 dex. The M_*–$M_{\rm halo}$ relations in Fig. 4 follow similar trends for the three models at different redshifts: a monotonically increasing relation with changes of slope at low, ≈$10^{10.7}$ M$_\odot$, and high, ≈10^{12} M$_\odot$, halo mass. The M_*–$M_{\rm halo}$ relation flattens out at $M_* < 10^{8.5}\,{\rm M}_\odot$ because no limit is imposed on the minimum halo mass. The change in slope at ≈10^{12} M$_\odot$ is mostly related to AGN feedback and the cooling recipes (Bower et al. 2012; Crain et al. 2015). For all three models, AGN feedback becomes effective for galaxies hosted by haloes with ≈10^{12} M$_\odot$. Up to the moment when a halo reaches ≈10^{12} M$_\odot$, the stellar mass growth of the galaxy within the halo is mainly driven by

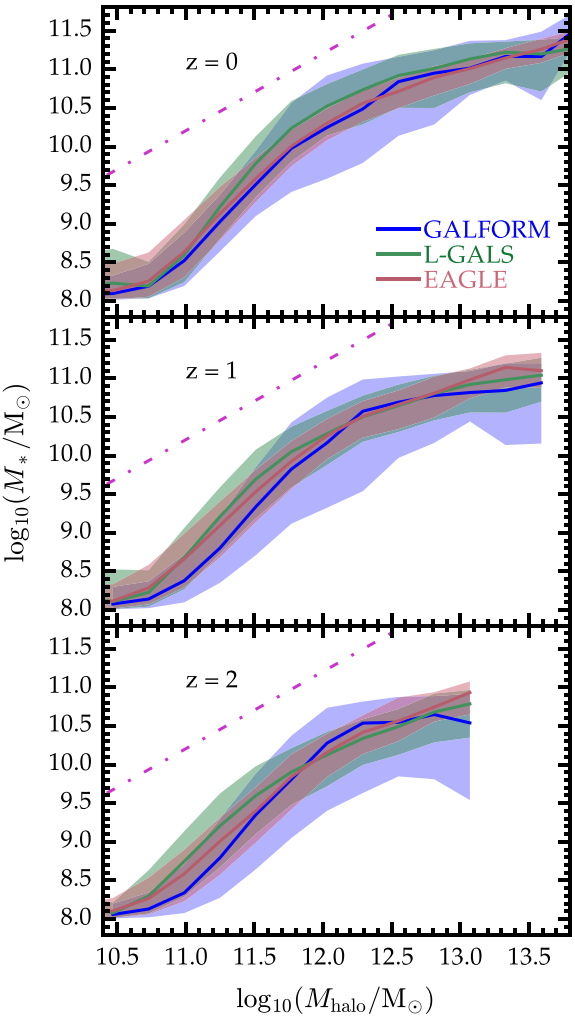

Figure 4. The stellar mass–halo mass relation (M_*–$M_{\rm halo}$) for central galaxies with masses above 10^8 $M_\odot$, predicted by EAGLE, GALFORM and L-GALAXIES at three redshifts, as indicated by the legend (see the appendix for a discussion of the halo mass definition). The filled regions show the 10th and 90th percentiles of each distribution, while the solid lines show the medians. The sloping magenta dash–dotted lines show the result of multiplying the halo mass by the universal baryonic fraction. At high masses, the stellar growth is driven by that stellar mass accreted during mergers, flattening the M_*–$M_{\rm halo}$ relation. The scatter in this relation is larger for GALFORM because (i) its AGN feedback depends more strongly on the accretion history of haloes and (ii) its stellar feedback efficiency is different in bulges and discs.

the consumption of available gas, hence the feedback from SNe is very important (e.g. Guo & White 2008). However, the AGN feedback prevents this growth channel from being effective, so mergers become the main driver for any further growth in stellar mass, flattening the M_*–$M_{\rm halo}$ relation. Given that the slope is shallower than unity, it is expected that minor mergers are the most important contributors to the stellar mass growth of massive galaxies. Even in the absence of AGN feedback, the stellar mass growth is expected to be slower for very massive haloes due to the increasing cooling times of massive haloes (e.g. Cowie & Binney 1977; Silk 1977; Lu et al. 2011a; Monaco et al. 2014). For GALFORM, we find that in the absence of AGN feedback the change in the slope of the M_*–$M_{\rm halo}$ relation happens at $\approx 10^{12.5}$ $M_\odot$.

The normalization, slope and scatter of the median M_*–$M_{\rm halo}$ relations shown in Fig. 4 mainly depend on the particular implementation of the stellar and AGN feedback. Thus, as expected, Fig. 4 shows differences between the models that vary with the halo mass. At $z = 0$, L-GALAXIES has a steeper slope in the range $10^{10.75} < M_{\rm halo}/{\rm M}_\odot < 10^{12}$ than the other two models. This gives rise to more massive galaxies at a given host halo mass above 10^{11} $M_\odot$. These aspects suggest that L-GALAXIES has weaker AGN feedback than the other models.

The scatter in the M_*–$M_{\rm halo}$ relation for haloes in the EAGLE simulation with $M_{\rm halo} \gtrsim 10^{11}$ $M_\odot$, remains almost constant with redshift at ≈0.3 dex. For haloes in L-GALAXIES with $M_{\rm halo} \approx 10^{11.5}$ $M_\odot$, the scatter of the M_*–$M_{\rm halo}$ relation decreases from ≈0.5 dex at $z = 2$ to ≈0.3 dex at $z = 0$, while it remains approximately constant ≈0.3 dex for haloes with $M_{\rm halo} \approx 10^{12}$ $M_\odot$. For haloes with $M_{\rm halo} \gtrsim 10^{12}$ $M_\odot$, the scatter in the distribution for the GALFORM model is ≈0.8 dex, and thus, larger than that for the other two models. In this range of high masses there are two aspects directly affecting the large scatter seen for the GALFORM model. The first one is that the efficiency of the AGN feedback in this model depends more strongly on the accretion history of haloes, because the effect of AGN feedback explicitly depends on the ratio of the halo cooling to dynamical time, taking into account the halo formation history (Bower et al. 2006, 2012). The second aspect is related to GALFORM having different stellar feedback efficiencies in bulges and discs, as described in Section 2.2.2, while L-GALAXIES assumes the SN mass loading depends on the halo maximum circular velocity, which is naturally more tightly correlated with the mass of the host halo. This difference results in a greater scatter at $M_{\rm halo} \gtrsim 10^{12}$ $M_\odot$ in the M_*–$M_{\rm halo}$ relation for GALFORM than for L-GALAXIES (Mitchell et al. 2016). Lowering the efficiency of the stellar feedback reduces the scatter in Fig. 4 for GALFORM, while increasing the normalization for small haloes.

3.3.1 *The mean halo occupation distribution*

The mean number of galaxies per halo, $\langle N \rangle_M$, which satisfy a particular selection criterion, as a function of halo mass is directly related to the one-halo term for the clustering of those galaxies (e.g. Benson et al. 2000). In Fig. 5, we compare $\langle N \rangle_M$ for galaxies with stellar mass $M_* > 10^{9.5}$ $M_\odot$ from the three models, at different redshifts. This stellar mass cut is chosen so that we can further separate galaxies into star-forming and passive categories, taking into account the resolution limits in EAGLE, as described in Section 2.3.

Galaxies with $M_* > 10^{9.5}$ $M_\odot$ start to appear in haloes of minimum mass $M_* \approx 10^{11}$ $M_\odot$, consistent with the stellar mass–halo mass relation shown in Fig. 4. The predicted $\langle N \rangle_M$ for galaxies chosen with different cuts in stellar mass follow similar trends to those shown in Fig. 5. However, the higher the cut in stellar mass, the more massive the host haloes are.

The top panels in Fig. 5 show the $\langle N \rangle_M$ separated into central and satellite galaxies, while the bottom panels show $\langle N \rangle_M$ of star-forming and passive galaxies (see Section 2.3 for the definition of the split). The $\langle N \rangle_M$ for central galaxies is close to a unit step function, which indicates that for a massive enough halo we can always find one central galaxy more massive than $M_* = 10^{9.5}$ $M_\odot$. This does not hold if either the cut in stellar mass is set to $M_* \gtrsim 10^{10.5}$ $M_\odot$ or if additional cuts are applied, such as in colour. In both cases, a decline in the $\langle N \rangle_M$ for central galaxies is expected, since galaxies selected in such a way will be less common (e.g. Gonzalez-Perez et al. 2011; Zehavi et al. 2011).

As shown in Fig. 5, the $\langle N \rangle_M$ for satellite galaxies is basically a power law beginning at halo masses about an order of magnitude larger than the minimum mass required to host a central galaxy at a

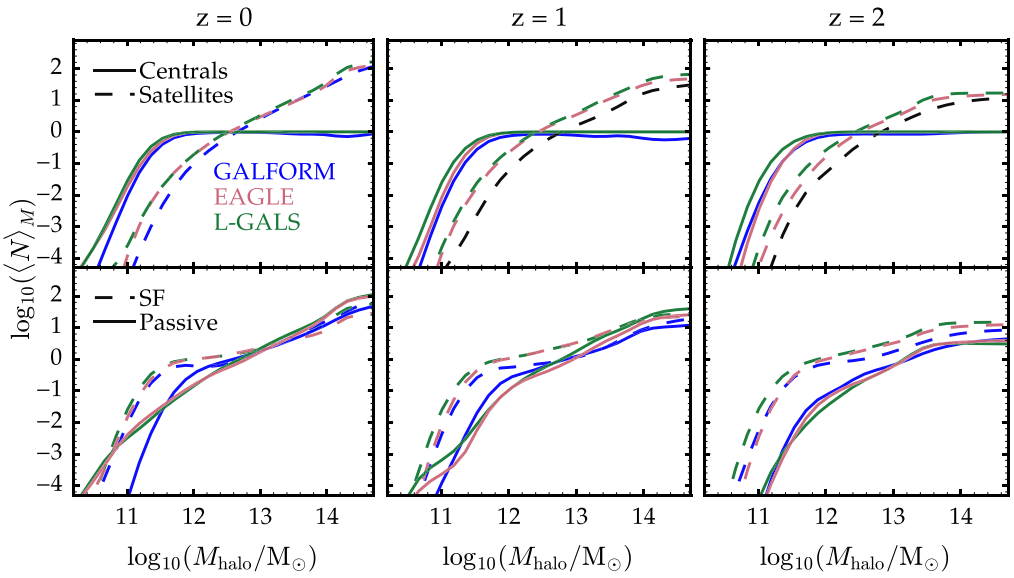

Figure 5. The mean number of galaxies per halo, $\langle N\rangle_M$, of galaxies more massive than $M_* > 10^{9.5}$ M$_\odot$ in EAGLE, GALFORM and L-GALAXIES at different redshifts, from left to right: $z = 0$, 1, 2. Top panels show the $\langle N\rangle_M$ of galaxies separated into centrals (solid lines) and satellites (dashed lines). Bottom panels show the $\langle N\rangle_M$ of galaxies separated into passive (solid lines) and star-forming (dashed lines, see Fig. 7 in Section 5). Differences in $\langle N\rangle_M$ between the three models are below 0.5 dex, except for the minimum halo mass required to host passive galaxies. This larger difference is related to the population of ejected satellites discussed in Section 2.3.

given redshift. The three models predict comparable trends for both central and satellite galaxies. At $z = 0$, the difference in numbers is less than 0.5 dex. This difference between GALFORM and the other two models, increases to ∼0.8 at $z = 2$, for most of the mass range covered.

The bottom-left panel in Fig. 5 shows that at $z = 0$ and in haloes with masses $\gtrsim 10^{12.5}$ M$_\odot$ the contribution from passive and star-forming galaxies to the global $\langle N\rangle_M$ is comparable (values within 0.5 dex). This is not the case when an instantaneous stripping of the hot gas in satellites is assumed in GALFORM (not shown). In this case, most satellites become passive very quickly, which translates into a $\langle N\rangle_M$ dominated by passive galaxies also at the massive end.

At $z = 0$, passive galaxies in GALFORM populate larger haloes than in either L-GALAXIES or EAGLE. The same is true for central galaxies, although the difference is smaller. This is directly related to the different assignment of galaxies to haloes as was discussed in Section 3.1.1. Changes in the parameters controlling the feedback in GALFORM have an impact on the minimum halo mass for hosting a galaxy above a given mass. Thus, the small differences, ≈0.2 dex, in the $\langle N\rangle_M$ of star-forming galaxies derived with the three models under study are at least partly driven by the differences in the efficiency of the stellar feedback and also by the treatment of mergers, as was discussed by Contreras et al. (2013).

4 THE COSMIC SFR DENSITY

The predicted evolution of the SFRD is shown in Fig. 6 for galaxies with $M_* > 10^8$ M$_\odot$, for the three models (see section Section 2.3 for a discussion on the stellar mass limits). We find that the SFRD is dominated by star-forming galaxies with stellar masses around the knee of the GSMF, $M_* \approx 10^{10.5}$ M$_\odot$ (not shown). Thus, the contribution to the global SFRD from galaxies with $M_* < 10^8$ M$_\odot$ is negligible.

The general shape of the predicted SFRD evolution is similar for the EAGLE, GALFORM and L-GALAXIES models, with a rise from $z = 0$ to about $z \approx 2.5$ and a decline at higher redshifts, as shown in Fig. 6.

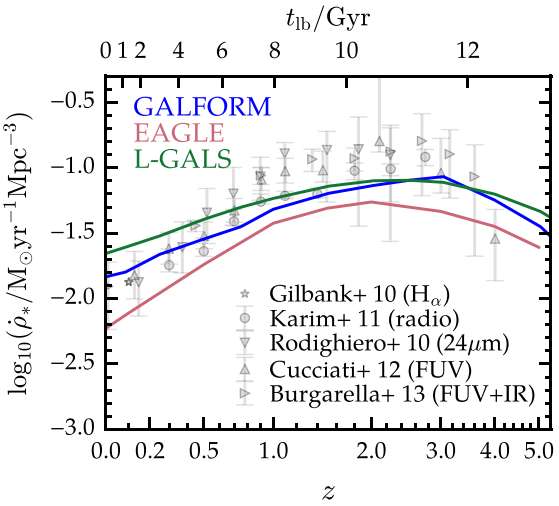

Figure 6. The evolution of the cosmic star formation rate per unit comoving volume (SFRD) of galaxies with stellar masses $M_* > 10^8$ M$_\odot$ predicted by EAGLE, GALFORM and L-GALAXIES, as indicated by the legend. For reference, the grey symbols present the observational results from Gilbank et al. (2010), which are based on Hα measurements, Rodighiero et al. (2010), based on 24 μm, the radio measurements from Karim et al. (2011), the FUV measurements from Cucciati et al. (2012), and the combined FUV+FIR measurements from Burgarella et al. (2013). When necessary, the data have been converted to a Chabrier IMF and Planck cosmology. The slope of the SFRD between $z = 0$ and 1 in EAGLE is about a factor of 1.5 steeper than those from the two SA models. This suggests that some of the physical processes that evolve with cosmic time in EAGLE do not evolve as much in the two SA models.

However there are important quantitative differences between the models.

The normalization of the SFRD is different for the three models, with a difference at $z = 0$ of a factor of 3.5 between EAGLE and

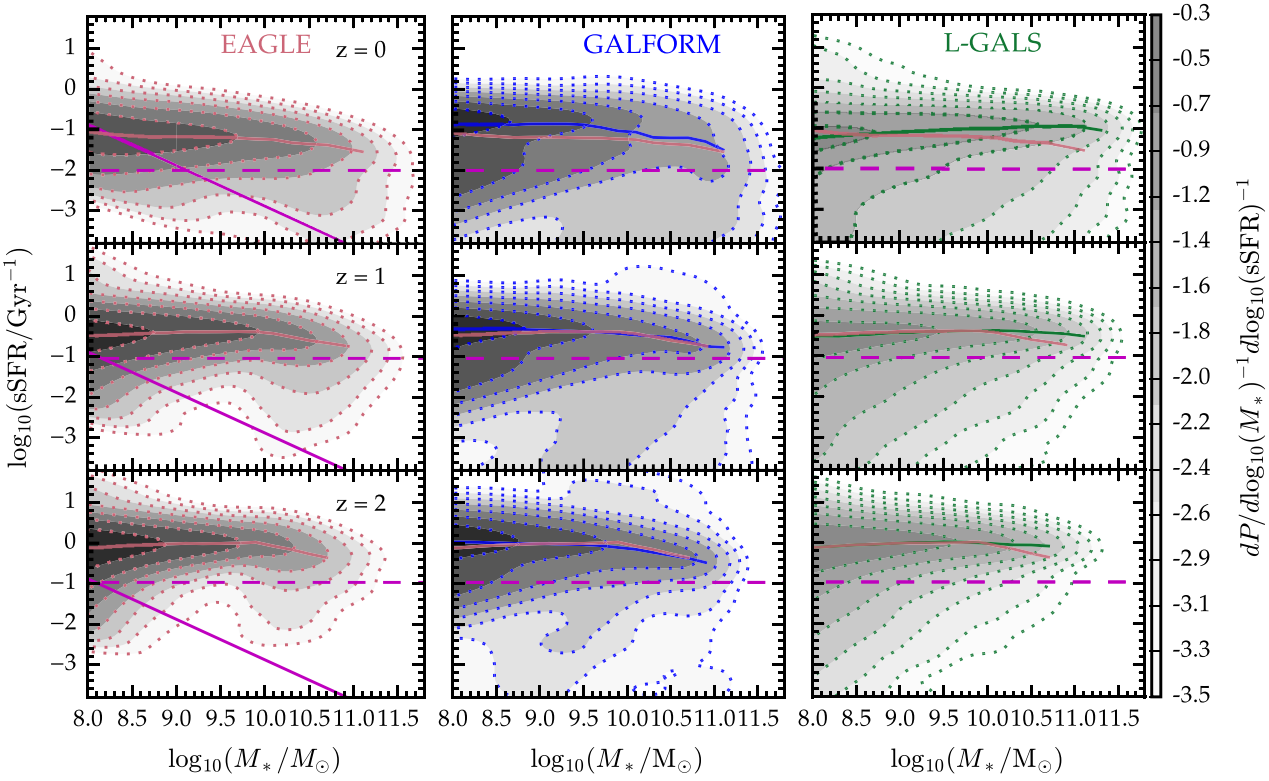

Figure 7. The probability densities of all galaxies as a function of sSFR and stellar mass predicted by EAGLE, left-hand column, GALFORM, middle column, and L-GALAXIES, right-hand column, at three redshifts, as indicated by the legend. The contours correspond to number densities divided by the total number of galaxies in the sample. The magenta horizontal dashed lines separate galaxies into star-forming, above, and passive galaxies, below. These lines are placed at $\log_{10}(\mathrm{sSFR/Gyr^{-1}}) = -2, -1.04, -0.97$ for $z = 0, 1, 2$, respectively. The median sSFR of star-forming galaxies as a function of stellar mass is shown as a solid red line for EAGLE (in all panels), a solid blue line for GALFORM and a solid green line for L-GALAXIES. The magenta sloping solid lines are a guide to the resolution of the EAGLE simulation, corresponding to the minimum stellar mass for galaxies with 30 SF particles resolving the sSFR value (see 2.3 for further details). Note that the intersection between the guide to EAGLE resolution, magenta sloping solid lines, and the boundary between passive and star-forming galaxies, magenta horizontal dashed lines, evolves with redshift due to the evolving sSFR limit. The median sSFR of star-forming galaxies is remarkably similar for the three models, and the small variations shown are driven by differences in the feedback efficiency.

L-GALAXIES and of 2.5 between EAGLE and GALFORM. The difference in normalization between EAGLE and the two SA models is relatively persistent at $z < 5.0$. The SFRD at $z = 0$ differs by a factor of 1.5 between GALFORM and L-GALAXIES, converging at $1 < z < 3.5$.

The peak of the SFRD is predicted to occur later in the EAGLE model, $z_{\rm peak} \approx 2$, than in either GALFORM or L-GALAXIES, $z_{\rm peak} \approx 3$. The slopes of the SFRD between $z = 0$ and the corresponding $z_{\rm peak}$ are about a factor of 2 flatter for the two SA models compared to EAGLE (this factor is reduced to ≈1.5 in the redshift range $0 < z < 1$). Thus, in EAGLE the growth of the stellar mass is delayed with respect to the SA models, but then the star formation quenching happens faster.

We have not found a satisfactory explanation for this difference by varying the free parameters in GALFORM that control either the gas cooling or the efficiency of the feedback processes. The slope of the SFRD evolution in EAGLE is influenced by processes that evolve with time due to the changing characteristics of the ISM and the intergalactic medium. These processes, while naturally incorporated in EAGLE, need an explicit modelling in the two SA models. Some aspects that have been suggested to evolve with time are the cooling of gas in massive haloes (Dekel et al. 2009), the associated effect on the efficiency of AGN feedback (van de Voort & Schaye 2012), the stellar-driven outflows (Hopkins et al. 2014) and the reincorporation time-scale of gas (Mitchell et al. 2014; Henriques et al. 2015). On these last two points, Hirschmann, De Lucia & Fontanot (2016) showed that the evolution in time of the gas reincorporation time-scales is not captured in the SA models used in this work. This aspect is fundamental for the evolution of galaxies and a more detailed analysis of outflows should be made in comparison to observations, in order to find a model that captures more realistically the behaviour of gas flows.

5 SPECIFIC SFRs

The sSFR (the SFR per unit stellar mass in a galaxy, $\mathrm{sSFR} = \mathrm{SFR}/M_*$) gives a measure of the inverse of the time-scale a galaxy requires to assemble its stellar mass *in situ* by a constant SFR. The distribution of the predicted sSFR as a function of stellar mass for EAGLE, GALFORM and L-GALAXIES are shown in Fig. 7, at redshifts 0, 1 and 2. For all three models, this distribution is dominated by galaxies with sSFRs between ≈0.1 and 10 $\mathrm{Gyr^{-1}}$ across two orders of magnitude in stellar mass. A drop in the sSFR distribution at high masses is also seen in Fig. 7, $M_* > 10^{9.5}\,\mathrm{M_\odot}$, for GALFORM and EAGLE. This is related, at least in part, to the fact that in this regime, the same mass haloes can host galaxies with very different SFRs, depending on the activity history of their central BH (Bower et al., in preparation).

5.1 The star-forming sequence

The median sSFRs of star-forming galaxies from EAGLE, L-GALAXIES and GALFORM at $z = 0, 1, 2$, are shown in Fig. 7 as solid lines. The scatter in the sSFR of star-forming galaxies at a given stellar mass is similar among the three models, although the range is marginally larger for $M_* < 10^9\,\mathrm{M}_\odot$ in the L-GALAXIES model. We have tested the impact of varying the sSFR cut by up to 1 dex below the chosen boundary values (see Section 2.3) and it does not change the global trends reported here for L-GALAXIES.

The median sSFR for star-forming galaxies remains remarkably constant with increasing stellar mass for all three models in the studied stellar mass range. Previous comparisons with observations have shown that model star-forming galaxies have a too flat median sSFR as a function of stellar mass (e.g. Weinmann et al. 2012; Mitchell et al. 2014; Furlong et al. 2015b).

At $z = 1$ and 2 the models agree within ≈0.2 dex. However, at $z = 0$, GALFORM predicts a median sSFR that is ≈0.4 dex higher than that of EAGLE and L-GALAXIES for galaxies with $M_* < 9.5\,\mathrm{M}_\odot$. In this stellar mass range, the GSMF in GALFORM is dominated by star-forming galaxies, with number densities larger than for the other models (see Fig. 2). This suggests that the stellar feedback in GALFORM is weaker than in EAGLE and L-GALAXIES, although, given that the difference is only found at $z = 0$, a more detailed study should be made in order to understand the origin of this difference.

Further, at all redshifts and above $M_* > 10^{10}\,\mathrm{M}_\odot$ there is a weak trend for the median sSFR to decrease with stellar mass for EAGLE and GALFORM, which is not seen for L-GALAXIES. The median sSFR for star-forming galaxies predicted by the L-GALAXIES model is similar to those predicted by the other two models below $10^{9.5}\,\mathrm{M}_\odot$ but the difference increases with stellar mass to a factor of ∼3 for galaxies with $M_* = 10^{11}\,\mathrm{M}_\odot$ at $z = 0$, being the largest at this redshift. Reducing the AGN feedback efficiency in GALFORM increases the median sSFR for $M_* \gtrsim 10^{10}\,\mathrm{M}_\odot$ at $z = 0$, while leaving it unchanged at lower stellar masses. Moreover, from Fig. 2 it is clear that at $z = 0$ the abundance of star-forming central galaxies around the knee of the GSMF, $M_* \approx 10^{10.75}\,\mathrm{M}_\odot$, is larger for L-GALAXIES than for the other two models. As shown in Fig. 4, these galaxies are also hosted by less massive haloes in L-GALAXIES, compared with the other two models. Both aspects are directly connected with L-GALAXIES having a weaker AGN feedback, allowing for a higher fraction of massive, $M_* > 10^{10.5}\,\mathrm{M}_\odot$, star-forming central galaxies at $z = 0$ which are hosted by haloes with $M_* \approx 10^{12}\,\mathrm{M}_\odot$. Thus, a weaker AGN feedback could explain the difference between L-GALAXIES and the other models.

5.2 The passive fraction

In both EAGLE and L-GALAXIES there are galaxies with SFR = 0 and $M_* > 10^8\,\mathrm{M}_\odot$ (over 25 per cent at $z = 0$). The existence of these galaxies is the result of both the finite resolution of the simulation and the threshold in cold gas density imposed for the formation of stars (see Section 2 for further details). At any redshift, less than 1 per cent of GALFORM galaxies has SFR below $10^{-5}\,\mathrm{Gyr}^{-1}$. Most of the galaxies with low sSFR are star-forming discs, for which GALFORM assumes the surface SFR density to be proportional to the molecular surface density (Lagos et al. 2011). This aspect is critical since all galaxies will convert some of their gas into H_2, resulting in a non-zero SFR as opposed to the modelling done in both EAGLE and L-GALAXIES.

Besides those galaxies with SFR = 0, it can be seen in Fig. 7 that both GALFORM and L-GALAXIES predict a relatively larger spread of passive galaxies with sSFR varying from 0.01 to $10^{-5}\,\mathrm{Gyr}^{-1}$. However, most passive galaxies in EAGLE have sSFR from 0.01 to $\approx 10^{-4}\,\mathrm{Gyr}^{-1}$. This reduced range is due to the minimum SFR that can be resolved in the EAGLE simulation, which depends on the mass resolution and the density threshold for star formation (Schaye et al. 2015).

The fraction of passive galaxies across cosmic time results from the interplay of the different physical processes that quench star formation in galaxies, such stellar and AGN feedback and environmental processes like ram-pressure stripping of hot gas. The fraction of passive galaxies as a function of stellar mass is shown in Fig. 8 for EAGLE, GALFORM and L-GALAXIES at $z = 0, 1$ and 2. The three models predict a global increase of the passive fraction with cosmic time.

For $z < 2$ and $M_* \gtrsim 10^{10}\,\mathrm{M}_\odot$, the three models predict the passive fraction to increase monotonically with stellar mass. At $z = 2$, the same is true for GALFORM, while both EAGLE and L-GALAXIES predict a rather flat fraction of passive galaxies that remains below 20 per cent for the whole population, and below 40 per cent for satellites. The strength of the AGN feedback impacts the number of massive passive galaxies and drives, at least partially, the differences between models at the massive end. GALFORM has the strongest AGN feedback of the three models, producing a larger fraction of passive and massive, $M_* \gtrsim 10^{11}\,\mathrm{M}_\odot$, galaxies, while L-GALAXIES has the weakest AGN feedback and thus has the lowest fraction. The stellar feedback can also impact the slope of the passive fraction at the massive end. In the GALFORM model, the gas mass heated by stellar feedback is directly dependent on the circular velocity of the disc, which is used as a proxy for the gravitational potential. However, for massive galaxies, the tight relation between the circular velocity in discs and their host haloes disappears, affecting the passive fraction slope for $M_* \gtrsim 10^{10}\,\mathrm{M}_\odot$.

The EAGLE simulation predicts the passive fraction to have a minimum $M_* \sim 10^{10}\,\mathrm{M}_\odot$ at $z = 0$ and $M_* \sim 10^{9.5}\,\mathrm{M}_\odot$ at $z = 1$. The passive fraction below these stellar masses is however strongly affected by sampling, due to the SFR and feedback being quantised, which gives rise to numerical effects (Furlong et al. 2015b).

At $z = 0$, GALFORM predicts a smaller number of low-mass passive galaxies relative to the other models. This is related to the higher number density of low-mass star-forming galaxies seen in Fig. 2 and, at least partly, a consequence of GALFORM galaxies experiencing a less efficient stellar feedback than in the other models. This also results in lower fractions of passive satellite and central GALFORM galaxies at $z = 0$, in relation to the other two models.

The number of low-mass passive central galaxies is smaller in GALFORM relative to the other models, as expected from the GSMF shown in Fig. 2. Besides the different stellar feedback efficiency, this variation is also related to the ejected satellite galaxies being classified as either centrals or satellites, as described in Section 3.1.1. As seen in Fig. 2, there is an increase in low-mass passive central galaxies in EAGLE and L-GALAXIES, relative to GALFORM, though this mainly happens below the EAGLE resolution limit.

For galaxies with $M_* < 10^{10}\,\mathrm{M}_\odot$, the fraction of passive satellites is larger than for central galaxies at all redshifts. The difference is reduced for higher stellar mass galaxies, with passive fractions being similar between central and satellite galaxies for $M_* > 10^{11}\,\mathrm{M}_\odot$ at $z = 0$ and $z = 1$, and at $z = 2$ also, in the case of L-GALAXIES. At $z = 2$, the fraction of passive and massive central galaxies is larger than for satellites in both EAGLE and GALFORM. The high-mass end of the passive fraction is mostly shaped by the AGN feedback.

By default, in the GALFORM model used for this study we are assuming a gradual stripping of the hot gas in satellite galaxies. If

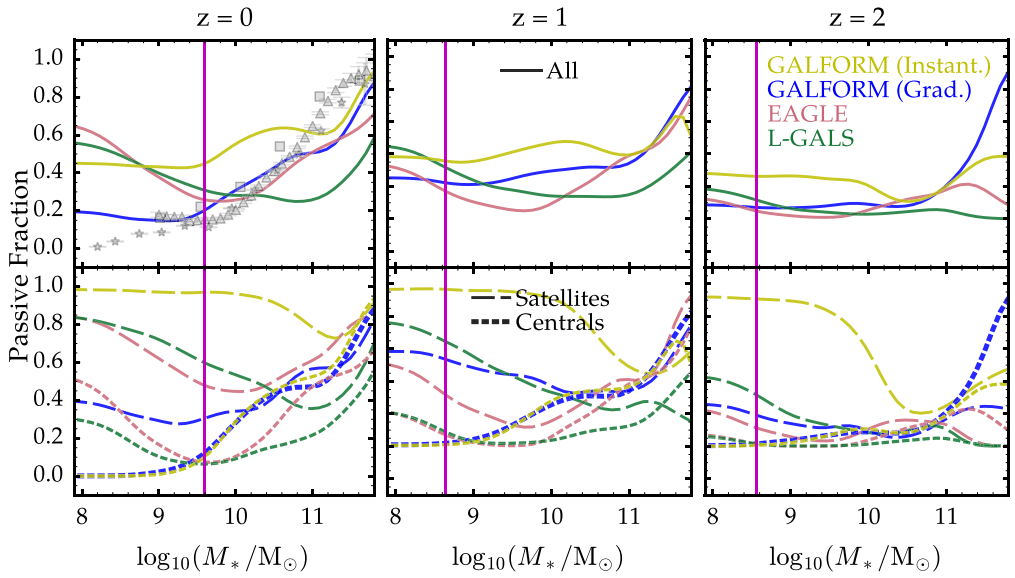

Figure 8. The fraction of passive galaxies as a function of stellar mass, predicted by EAGLE, GALFORM and L-GALAXIES at different redshifts, as indicated by the legend. The top panels show the passive fractions for all galaxies, while the bottom panels shows separately the contributions from central (dotted lines) and satellite galaxies (dashed lines). In this plot, we show the predictions from GALFORM assuming either gradual ('Grad.', blue lines, the default model in this paper) or instantaneous ram-pressure stripping ('Instant.', yellow lines) of the hot gas in satellite galaxies. The magenta vertical lines are a guide to the resolution limits of EAGLE, note that these evolve with redshift due to an evolving sSFR limit (see Section 2.3). For reference, observational passive fractions based on either colour or sSFR cuts are plotted as grey stars (Gilbank et al. 2010), triangles (Moustakas et al. 2013) and squares (Bauer et al. 2013). The passive fraction increases with cosmic time. The increase in the fraction of low-mass passive galaxies in EAGLE and L-GALAXIES is driven, at least in part, by the population of ejected satellites discussed in Section 3.1.1.

instead an instantaneous stripping is assumed, the passive fraction of satellites rises to 100 per cent below a threshold stellar mass which evolves to higher values at lower redshifts, being around 10^{10} $M_\odot$ at $z = 0$. This also affects the global passive fraction predicted by GALFORM, which is then close to 40 per cent for low-mass galaxies at $z = 0$, instead of the 20 per cent, shown in Fig. 8.

5.3 The evolution of the sSFR

In Fig. 9, we explore the evolution of the median sSFR with cosmic time. Previous studies using SA models have shown that the stellar mass growth for galaxies of a given final mass roughly follows that of the dark matter component but with a normalization that varies with mass (Mitchell et al. 2014). From *N*-body simulations of ΛCDM cosmologies, the dark matter halo mass has been found to grow with redshift roughly as a power law in scalefactor and have little dependence on halo mass (Wechsler et al. 2002; Genel et al. 2008; Fakhouri, Ma & Boylan-Kolchin 2010). Recently, Correa et al. (2015) derived the halo mass accretion history from the growth rate of initial density perturbations, by using the extended Press–Schechter approach (e.g. Lacey & Cole 1993; Neistein, van den Bosch & Dekel 2006). In Fig. 9, we show the median sSFR of star-forming galaxies normalized by the specific accretion rate of the typical haloes hosting the galaxies of interest, $t_{\rm growth}^{-1}$. This specific accretion rate is calculated from

$$t_{\rm growth}^{-1} = \frac{{\rm d}M/{\rm d}t}{M(z)}, \quad (2)$$

$$M(z) = M_0(1+z)^{\alpha} e^{\beta z}, \quad (3)$$

where M_0 is the final halo mass and both α and β are functions of M_0 (see Correa et al. 2015, for further details). We note that, although we use the analytical scaling equations presented in Correa et al. (2015), similar trends and conclusions are reached when using the approximations provided by either Genel et al. (2008) or Fakhouri et al. (2010).

In Fig. 9, we separated galaxies into three stellar mass ranges. We are interested in comparing the SFRs of galaxies in each of these ranges with the expected mass assembly rate of their typical host halo. Thus, here we set M_0 at each redshift to be equal to the average mass of the haloes hosting galaxies with stellar masses within each bin shown in Fig. 9. Although some bias can be introduced by doing this, for the purpose of providing a rough estimate of how closely the sSFR follows the evolution of < the mass accretion rate of dark matter haloes, this is a reasonable approximation. In fact, to explore in detail the build-up of the mass for galaxies in different final stellar mass bins, individual haloes should be followed across time (Mitchell et al. 2014).

The first thing to note from Fig. 9 is that the predicted sSFR· $t_{\rm growth}$ is reasonably flat for all the default models, with slopes $<\pm 0.4\,{\rm Gyr}^{-1}$. This implies that the star formation histories of model galaxies closely follow the mean mass assembly rate expected from their dark matter host haloes and that the differences between the models are minimal. In the SA models, the stellar mass assembly process broadly traces that of haloes because the mass loading and reincorporation efficiencies do not evolve significantly over the history of the galaxy for typical star-forming galaxies at $z < 1$ (see Mitchell et al. 2014, for details). What might be surprising, is that galaxies in EAGLE also follow the dark matter assembly quite closely. In EAGLE, the mass loading for SN feedback does not depend explicitly on dark matter or halo properties (Schaye et al. 2015), nevertheless the reincorporation time for reheated gas is expected to depend on the halo properties.

The sSFR tends to trace the dark matter assembly as a function of lookback time even for a wide range of variants of GALFORM (Mitchell et al. 2014). Nevertheless, we have found a very large

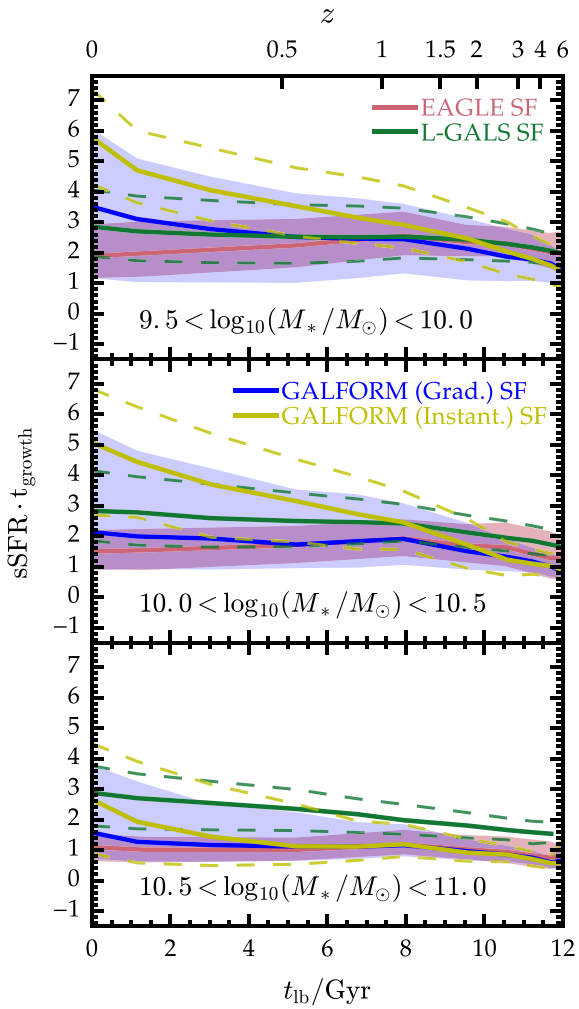

Figure 9. The median sSFR times the expected growth time-scale of the corresponding host haloes, as functions of lookback time for star-forming galaxies in EAGLE, GALFORM and L-GALAXIES (see the text in Section 5.3 for further details). The three panels show star-forming galaxies in different stellar mass bins of 0.5 dex width and centred at $\log_{10}(M_*/\mathrm{M}_\odot) = 9.75, 10.25, 10.75$, as indicated by the legend. The shadowed regions and dashed lines show the corresponding 25th and 75th percentiles of the distributions. The star-forming galaxies are classified according to the magenta horizontal lines in Fig. 7, which are interpolated to other redshifts. In this plot, we show the predictions from GALFORM assuming either gradual ('Grad.', blue lines, the default model in this paper) or instantaneous ram-pressure stripping ('Instant.', yellow lines) of the hot gas in satellite galaxies. Given the flatness of the relations shown in this figure, we can conclude that the evolution of the sSFR, in all the default models, closely follows the specific mass assembly history of their host dark matter haloes.

difference for the GALFORM prediction when assuming the stripping of hot gas in satellite galaxies to be instantaneous as opposed to of gradual (the default here), as seen in Fig. 9. The figure only shows star-forming galaxies, which in the case of the instantaneous stripping model, will be dominated by central galaxies given that in this model satellite galaxies are mostly passive. The scatter seen for the default GALFORM model is largely due to the contribution of star-forming satellite galaxies. These dominate the low stellar mass ranges at low redshift, as seen in Fig. 2. It is clear from this that the evolution of the stellar feedback in GALFORM is different from the other models, allowing for larger numbers of low-mass galaxies by adopting either a weaker stellar feedback or shorter reincorporation times.

5.4 The distribution of sSFR at a given stellar mass

Most of the stellar mass in the Universe at a given time is dominated by galaxies located around the knee of the GSMF ($M_* \approx M_{\rm Break}$). Thus, it is interesting to explore in more detail the distribution of sSFRs for these galaxies. As has been discussed in Section 3.1, the stellar mass corresponding to the knee of the GSMF depends on the model and, for a given model, it evolves with redshift. In order to approximately enclose the relevant range for the three models and redshifts, galaxies with $10^{10} < M_*/\mathrm{M}_\odot < 10^{11}$ are included in Fig. 10, separated into central and satellite galaxies. In this stellar mass range, the three models predict similar number densities at $z = 0$ and there are sufficient satellite galaxies to study the trends even at higher redshifts. Note that while we focus on $10^{10} < M_*/\mathrm{M}_\odot < 10^{11}$ here, the global trends and qualitative results are valid for stellar mass ranges selected from about $10^{9.3}$ to $10^{11.5}$ $\mathrm{M}_\odot$.

The three models present qualitatively similar distributions for both central and satellite galaxies (see Fig. 10), with galaxy numbers increasing with sSFR until a peak is reached at sSFR between 0.03 and 1 Gyr^{-1}. Beyond which, the number of galaxies declines. For the mass range shown in Fig. 10, the number of central galaxies with low sSFR in GALFORM is higher than for the other two models (over $\approx$1 dex for galaxies with sSFR$<10^{-3.5}$ Gyr^{-1}). This difference is related to both the lack of a threshold for the star formation in this model (see Section 5.2) and the details of the separation between central and satellite galaxies, which affects the number of passive centrals, as discussed in Section 3.1.1.

The peak of the sSFR distribution occurs at somewhat different values depending on the model. The sSFR medians increase with increasing redshift up to $z = 2$ (see Fig. 10), as the model SFRD does (see Fig. 6). The sSFR medians for central galaxies in L-GALAXIES is higher than that in the other two models at all redshifts for this stellar mass range, as expected from the difference seen for the median sSFR of massive galaxies (see Fig. 7).

5.4.1 *The sSFR as a function of environment*

The environment can be traced by different estimators, such as the host halo mass, kinematic parameters (Hahn et al. 2007; Hoffman et al. 2012; Libeskind et al. 2012), or the density (Sousbie 2011; Tempel et al. 2011). Here we use the host halo mass as the tracer of the environment and thus, we note that the results might change if a different definition is chosen. In the right-hand column of Fig. 10, we compare the effect that environment has on the sSFR of satellite galaxies as predicted by the three models.

We study satellite galaxies in the same range in stellar masses as in the middle column of Fig. 10, $10^{10} < M_*/\mathrm{M}_\odot < 10^{11}$, separating them into halo mass bins of $10^{12} < M_{\rm halo}/\mathrm{M}_\odot < 10^{13}$ and $10^{13} < M_{\rm halo}/\mathrm{M}_\odot < 10^{14}$. Modifying the stellar mass range of the satellites, choosing mass ranges within $10^{9.3} < M_*/\mathrm{M}_\odot < 10^{11}$, again does not change the results in this section. The same is true for the host halo mass, provided that the chosen haloes are massive enough to host the corresponding satellite galaxies.

Overall, the three models predict similar trends with environment (host halo mass, in this case). The differences between the models on average are less than 1 dex. For a given stellar mass range, satellite galaxies hosted by less massive haloes have slightly higher sSFRs than those hosted in more massive haloes. Correspondingly, at

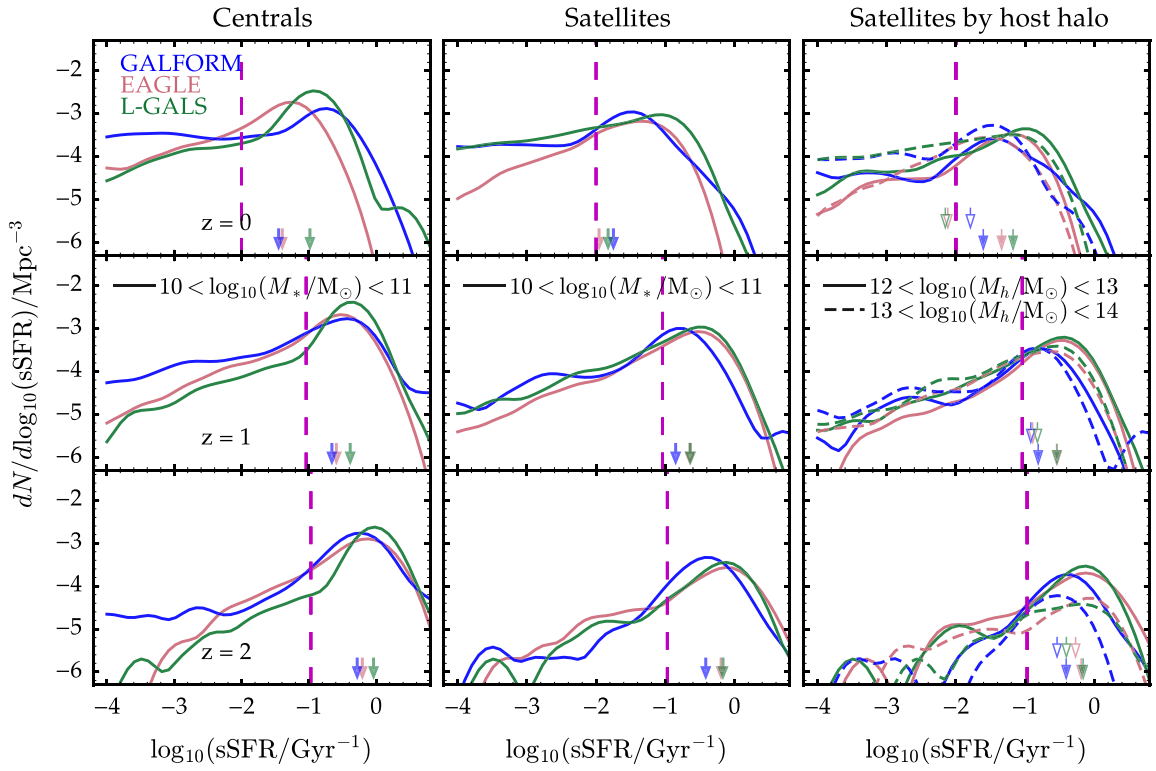

Figure 10. The comoving density of central, left-hand column, and satellite galaxies, central column, as a function of sSFR, for galaxies with $10^{10} < M_*/\mathrm{M}_\odot < 10^{11}$, for the three models at three redshifts, as indicated by the legend. The right-hand column shows the number density of satellite galaxies with $10^{10} < M_*/\mathrm{M}_\odot < 10^{11}$, hosted by haloes with $10^{12} < M_{\rm halo}/\mathrm{M}_\odot < 10^{13}$ (solid lines) and by haloes with $10^{13} < M_{\rm halo}/\mathrm{M}_\odot < 10^{14}$ (dashed lines). In all the panels, the median sSFR for each model is shown by an arrow of the corresponding colour. In the right-hand column, the medians of the lower mass ranges are shown by filled arrows, while the high-mass ranges are shown by open ones. The dashed magenta vertical lines correspond to the chosen boundary between passive, left-hand side, and star-forming galaxies, right-hand side of the line (see also Fig. 7 and Section 2.3). Note from the right-hand column of this figure, that the median sSFR of satellite galaxies with $10^{10} < M_*/\mathrm{M}_\odot < 10^{11}$ declines with increasing host halo mass.

$z = 0$ the fraction of passive satellite galaxies is higher for more massive host haloes, though this trend is noisy due to the low numbers of passive galaxies. For the two host halo mass ranges, the stellar mass distributions differ by less than a factor of 3. Thus, the trends with environment seen for the sSFR of satellite galaxies are not driven by differences in stellar mass but are a reflection of the effect of environment (host halo mass) on the star formation in the three models.

6 METALLICITY

The metallicity reflects the history of the gas reprocessing by stars and the exchange of gas between a galaxy and its environment. Moreover, the metallicity affects the cooling of the gas, which is one of the fundamental aspects driving the efficiency and timing of star formation in galaxies. In this section, we compare predicted metallicities, defined as the ratio between the mass of metals and total mass. In the case of EAGLE, metallicities have been obtained by considering either all particles associated with a given galaxy or those that are star forming for the gas phase, as opposed to the aperture values applied to other properties.

An assumption that is made in the case of the SA models but not EAGLE, is the instantaneous recycling approximation, whereby all metals are returned immediately to the ISM following star formation. In EAGLE metals are returned to the ISM with a time delay which depends on their production time during stellar evolution. However, as the total Z_* and $Z_{\rm cold}$ are dominated by oxygen, the majority of which is released on short time-scales, this approximation is not bad at high redshifts, although the delayed contribution of intermediate mass stars is still neglected and this accounts for about half the metals at $z = 0$ (Segers et al. 2016).

6.1 The stellar mass–stellar metallicity relation

The stellar mass–stellar metallicity, M_*–Z_*, relations of galaxies from the three models at redshifts $z = 0$, 1, 2 are shown in Fig. 11. The models predict a stellar metallicity that increases with stellar mass at all redshift shown. At $z = 0$, the M_*–Z_* relation flattens for $M_* > 10^{10.5}\,\mathrm{M}_\odot$. For galaxies of $M_* \approx 10^{10.5}\,\mathrm{M}_\odot$ the median metallicities predicted by the three models are in marginal agreement (within ≈0.2 dex) at all redshifts. Nevertheless, across the full stellar mass range, the stellar metallicities predicted by the models vary significantly. At the range of redshift explored, the predicted slopes of the M_*–Z_* relations are different between the three models. The slope of the M_*–Z_* relation remains almost constant with redshift for both SA models, a slope of ≈0.6 for GALFORM and of 0.25 for L-GALAXIES. The slope of the M_*–Z_* relation varies in EAGLE from 0.32 at $z = 2$ to 0.14 at $z = 0$. The difference in slopes between the models produces a large variation in the median metallicities of low-mass galaxies. This variation is largest at $z = 0$. At this redshift, the median metallicity of galaxies with $M_* \approx 10^8\,\mathrm{M}_\odot$ differs by ≈0.5 dex between the EAGLE and L-GALAXIES and by ≈1.1 dex between EAGLE and GALFORM. Similar trends are found when we separate the sample into central and satellite galaxies.

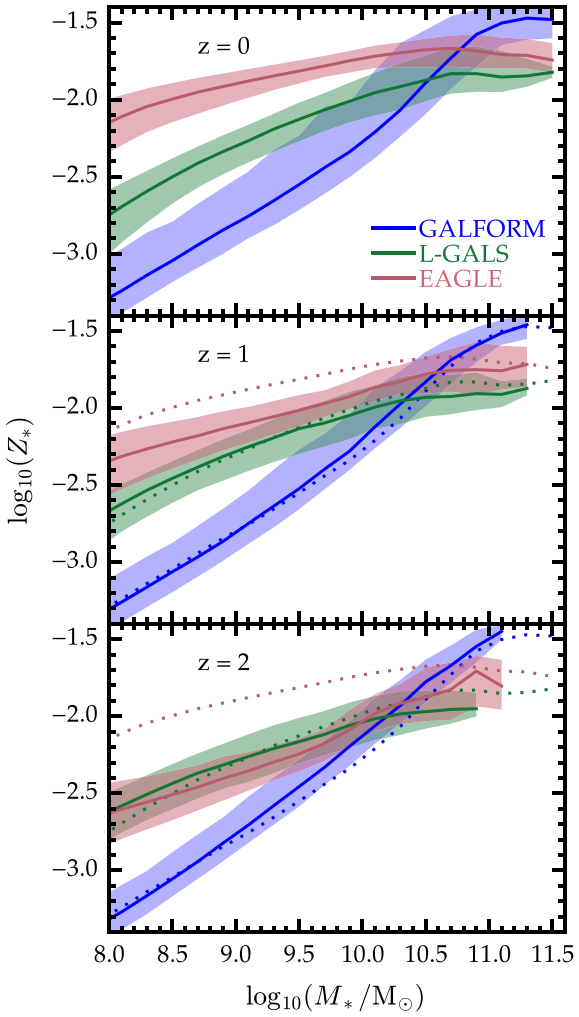

Figure 11. The stellar metallicity as a function of stellar mass, the M_*–Z_* relation, of galaxies in GALFORM, EAGLE and L-GALAXIES, at different redshifts, as indicated by the legend. The shaded regions show the corresponding 10th and 90th percentiles of the distribution. For reference, the median of the M_*–Z_* relation at $z = 0$ of each model is shown by dotted lines of the corresponding colour in the panels for $z = 1$ and 2. Note that the M_*–Z_* relation from EAGLE is not converged relative to higher resolution simulations (Schaye et al. 2015). The slope of the M_*–Z_* relation from EAGLE flattens with time and this is seen for both the reference run and the high resolution one, which is not shown in the figure. Meanwhile the slopes of the M_*–Z_* relation from two SA models remain practically unchanged with redshift.

Both the slope and the normalization of the M_*–Z_* relation are sensitive to the modelling of stellar feedback, and in the case of EAGLE for $M_* \gtrsim 10^{10}\,\mathrm{M}_\odot$, AGN feedback (Lacey et al. 2015; Schaye et al. 2015; Segers et al. 2016). Due to the very different ways in which hydrodynamic simulations and SA models treat metal enrichment and the transport of metals (Sections 2.1 and 2.2.2), these differences in the relations are unsurprising. In the two SA models, the stellar feedback can be reduced by either lowering the normalization of the mass-loading factor or by changing how it depends on the relevant velocity, as described in Section 2.2.2. Lowering the normalization of the mass-loading factor results in an increased normalization of the M_*–Z_* relation (Lacey et al. 2015), as is also found in EAGLE (Crain et al. 2015). However, a decrease in the slope of the dependence of mass loading on circular velocity allows small galaxies to retain a larger fraction of their metals, flattening out the M_*–Z_* relation (Lacey et al. 2015). In GALFORM, the AGN feedback has a marginal effect on the M_*–Z_* relation, while in EAGLE it can affect the massive end of this relation (Segers et al. 2016). At least at $z = 0$, the differences between EAGLE and the SA models are alleviated when the latter include a non-instantaneous approximation for the recycling of metals (Yates et al. 2013) and a higher resolution hydrodynamical simulation is used (Schaye et al. 2015).

An interesting difference between EAGLE and the SA models is the lack of evolution in the slope of the M_*–Z_* relation in the two SA models. This lack of evolution implies that, on average, the growth in metal mass follows almost exactly the growth in stellar mass, while this is not the case for EAGLE galaxies. In SA models, the differential recycling and metal retention effects are not properly accounted for (Ma et al. 2016). Stellar winds can affect the efficiency of stellar feedback and, in turn, the evolution of the metal retention in small galaxies. Winds in the SA models could be treated in a more realistic way, for example by using a dynamical model of SN feedback following the evolution of pressurised bubbles (Lagos, Lacey & Baugh 2013). We have tested that the pre-enrichment of the gas in haloes at late times has a minimal impact on the evolution of the M_*–Z_* relation. One aspect that may affects the evolution of this relation is the delayed metal enrichment that occurs in EAGLE, as opposed to the instantaneous recycling approximation assumed in the two SA models in this work, as the stellar feedback depends on the metal enrichment (Yates et al. 2013; De Lucia et al. 2014).

The treatment of metals in EAGLE is very different to that in SA models as the metals are associated with particles. Gas particles are enriched in a stochastic manner when in the vicinity of stars (Section 2.1), thus as winds are driven from the ISM the metals in the galaxy are redistributed. To partially account for the mixing of metals in the simulation, smoothed metallicities are computed using the SPH kernel of a particle (Wiersma et al. 2009b), however metal diffusion is not accounted for in the simulation. While aspects of the subgrid physics can be improved to account for the transport of metals, Schaye et al. (2015) have shown that the M_*–Z_* relation is not converged relative to higher resolution simulations. Such higher resolution simulations produce a steeper relation, at least at $z = 0$. Thus, to carry out a more detailed study of the metallicities relative to hydrodynamical simulations, converged results are required first.

6.2 The stellar mass-cold gas metallicity relation

In Fig. 12, we show the predicted stellar mass–cold gas metallicity, M_*–$Z_{\rm cold}$, relation for the three models at redshifts $z = 0$, 1 and 2. In particular, we show the gas-phase oxygen abundance for star-forming galaxies as this quantity is only measurable observationally for such galaxies (e.g. Tremonti et al. 2004; Zahid et al. 2013, 2014). The model $Z_{\rm cold}$ is converted to the gas-phase oxygen abundance shown in Fig. 12 assuming solar abundance ratios. Specifically, we assume that $Z_{\mathrm{M}_\odot} = 0.0134$ (Asplund et al. 2009) and $12 + \log_{10}(\mathrm{O/H})_{\mathrm{M}_\odot} = 8.69$ (Allende Prieto, Lambert & Asplund 2001). This selection of galaxies on or above the main sequence of star formation also ensures that their properties are well resolved in EAGLE. The gas-phase metallicity depends on the flows of gas in and out of a galaxy and on the stellar winds from dying stars and is thus expected to roughly follow the stellar metallicity but with more variability.

The models predict a gas-phase metallicity that increases with stellar mass for star-forming galaxies in a similar way to that shown

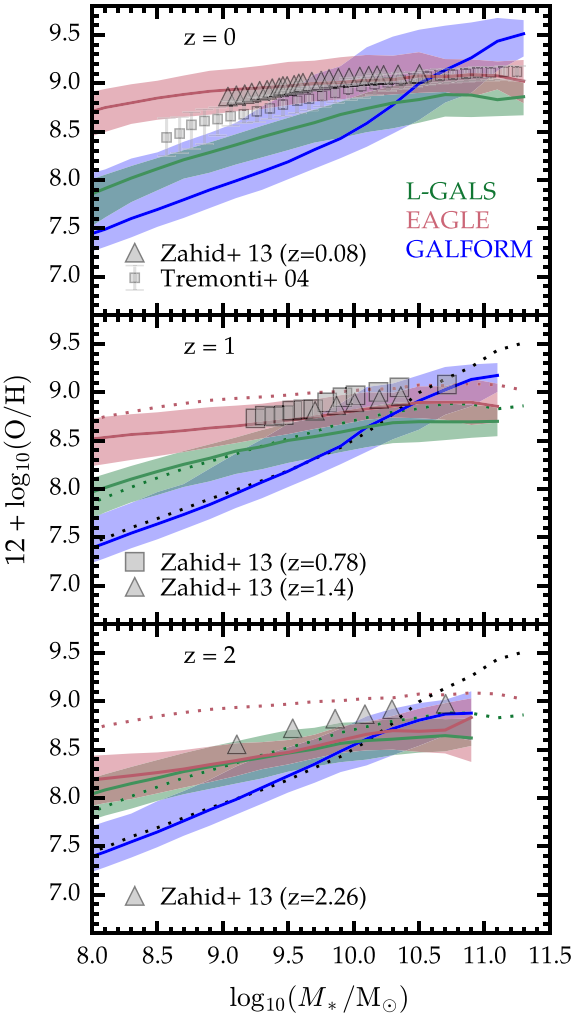

Figure 12. The cold gas metallicity (gas-phase oxygen abundance) as a function of stellar mass of star-forming galaxies, the M_*–$Z_{\rm cold}$ relation, in EAGLE, GALFORM and L-GALAXIES, at different redshifts, as indicated by the legend. The shaded regions show the corresponding 10th and 90th percentiles of the distribution. The median of M_*–$Z_{\rm cold}$ relation at $z = 0$ of each model is shown by dotted lines in the $z = 1$ and 2 panels. For reference, values derived from observations by Tremonti et al. (2004) and Zahid et al. (2013) have been included as grey symbols, as described in the legend. The M_*–$Z_{\rm cold}$ relations follow similar trends to the M_*–Z_* ones, but with larger spreads.

for the stellar metallicity in Fig. 11, although with a larger scatter, as expected. As for the stellar metallicity, we find little evolution for the gas-phase metallicity in the SA models, while EAGLE predicts a relation that flattens with increasing time and a small, ≈0.2 dex, increase in the mean metallicity.

The reasons that account for these differences are similar to those discussed in Section 6.1. In summary, the metallicities of simulated galaxies are found to be inconsistent across models, both as a function of stellar mass and redshift. To investigate these differences further, higher-resolution hydrodynamic simulations are required and more detailed modelling of metal production and redistribution should be considered in SA models.

7 GALAXY SIZES

In this section, we compare predicted galaxy sizes as measured by the 3D stellar half-mass radius, r_{50}. This quantity, although not available observationally,[4] is the most straightforward way to encapsulate the galaxy size and allows a fair and detailed comparison between the studied models.

Details on the calculation of galaxy sizes by the two SA models can be found in Section 2.2.2. In EAGLE, the r_{50} radius has been measured using a 3D aperture[5] of 30 proper kpc, as applied for the stellar mass and SFR measurements discussed previously.

In Fig. 13, we show the stellar mass–size, M_*–r_{50}, relation at $z = 0, 1, 2$ from EAGLE, GALFORM and L-GALAXIES. The dot–dashed horizontal lines indicate the gravitational force softening in EAGLE (see Table 1), below which galaxy sizes can be overestimated due to the suppression of the gravitational force at this limit. Note that this does not affect galaxies presented in this study across the redshift range considered. A point to recall before discussing the comparison between models is that in EAGLE the sizes of disc galaxies at $z \approx 0$ were considered in the calibration of the model (Table 3); however, the evolution of the galaxy sizes is a prediction from the model (see Furlong et al. 2015a, for a detailed study of the evolution of the galaxy sizes compared with observations).

The median M_*–r_{50} relations for the three models at $z = 0$ and 1 increase with stellar mass for $M_* \lesssim 10^{9.5}\,{\rm M}_\odot$, while GALFORM sizes decrease with increasing mass at $M_* \gtrsim 10^{9.5}\,{\rm M}_\odot$. At $z = 2$, L-GALAXIES sizes increase with stellar mass, the EAGLE relation flattens at $M_* \approx 10^{9.5}\,{\rm M}_\odot$ and decreases with stellar mass at higher masses, and the GALFORM sizes are reasonably flat with stellar mass at $M_* \lesssim 10^{9.5}\,{\rm M}_\odot$ and again decrease with increasing stellar mass at higher masses. In spite of differing trends with stellar mass, all three models predict that galaxy sizes decrease with increasing redshift. From $z = 2$ to 0, galaxies with $M_* \approx 10^{10}\,{\rm M}_\odot$ increase in size by ≈0.4 dex for the two SA models and by ≈0.2 dex for EAGLE. For all models, the galaxy sizes are found to be sensitive to the input physics, in particular the stellar feedback (e.g. Crain et al. 2015; Lacey et al. 2015).

The most notable difference between the models is the decrease in galaxy sizes with increasing stellar mass in the GALFORM model, which is not seen for L-GALAXIES and only seen at $z = 2$ for EAGLE, but in a milder form. The decrease in median size for the GALFORM galaxies is due to the particular modelling of the self-gravity of discs and how this affects the host dark matter halo (Section 2.2.2). While L-GALAXIES ignores the self-gravity of baryons and possible contraction of dark matter haloes due to it, GALFORM appears to overestimate these effects. The model of the self-gravity of baryons impacts galaxy sizes and this, in turn, affects the evolution of their star formation. Thus, this point is of crucial importance in understanding the evolution of galaxies. The comparison between EAGLE and the SA models highlights the need for a better analytic approximation of the effect that baryons have on the distribution of dark matter.

A further consideration in the SA model modelling of galaxy sizes that can account for some of the differences seen relative to EAGLE is the very simple assumptions made to model the angular momentum, in particular for mergers. The evolution of angular momentum, the

[4] For EAGLE, the projected half-mass radii for only disc galaxies (Sérsic index, $n_{\rm s} < 2.5$), which are calculated by fitting a Sérsic profile to projected and azimuthally averaged surface density profiles, are compared with the observations in fig. 9 of Schaye et al. (2015). For GALFORM, the predicted half-light radii as a function of r-band magnitude for early- and late-type galaxies are compared with the observations in fig. A3 of Gonzalez-Perez et al. (2014). For L-GALAXIES, the projected half-light radii for late-type galaxies are compared with observations in fig. 2 of Guo et al. (2011).

[5] See Furlong et al. (2015a) for a discussion of the change in galaxy sizes with aperture radii in EAGLE.

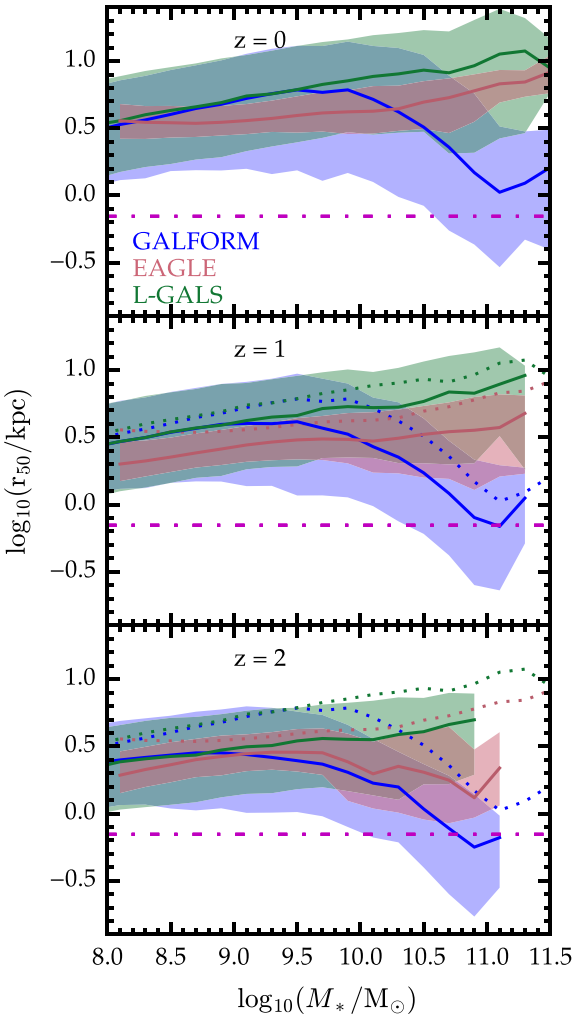

Figure 13. The median half-mass radius (r_{50}) as a function of stellar mass, the M_*–r_{50} relation, for galaxies in EAGLE, GALFORM and L-GALAXIES at different redshifts, as indicated by the legend. The shaded areas comprise the 10th to 90th percentiles of the distributions. The magenta horizontal dot–dashed lines indicate the scale of the gravitational softening used in the EAGLE simulation at different redshifts, which can be used as a resolution guide. For comparison, the median M_*–r_{50} relation at $z = 0$ for each model is also shown in the $z = 1$ and 2 panels, as dotted lines of the corresponding colour. At low-masses, the scatter in the M_*–r_{50} relation is very similar for the two SA models and about a factor of 2 larger than that for EAGLE. At high masses, the GALFORM M_*–r_{50} relation drops due to the modelling of the contraction of dark matter haloes caused by the self-gravity of baryons.

self-gravity of baryons and its effect on the dark matter are taken into account naturally by gas dynamics in hydrosimulations such an EAGLE. Although note that hydrodynamical simulations can suffer from angular losses resulting in sizes that are too small if efficient feedback in not implemented (Katz 1992; Navarro & White 1993; Crain et al. 2015).

In EAGLE, the decrease in galaxy sizes with increasing stellar mass at $z = 2$ for $M_* \gtrsim 10^{9.7}\,\mathrm{M}_\odot$ is not due to an aperture effect. This decline could be due to the highest mass galaxies at this redshift forming early when densities in the Universe were higher, thus forming compact cores. The comparison to the SA models suggest that the decline in the M_*–r_{50} relation at high redshift in EAGLE could also be the result of moving from a regime in which the self-gravity of baryons affects the concentration of the dark matter host haloes to a regime in which this effect is erased due to an important contribution from dissipationless mergers (Navarro & White 1993; Gao et al. 2004).

Another interesting difference between the models is the extent of the scatter in the M_*–r_{50} relation, which at $z = 0$ for $M_* < 10^{9.5}\,\mathrm{M}_\odot$ ranges from ≈0.2 dex in EAGLE, to ≈0.4 dex for the two SA models. Separating the galaxy sample by morphology, we find that the scatter in the relation in GALFORM is larger for bulge dominated galaxies than for discs, but for the latter the range still covers ≈0.4 dex. Thus, the difference in the extent of the scatter between the two SA models and EAGLE might point to a more fundamental aspect of the modelling related to how the angular momentum of discs is tracked. Exploring this possibility further requires a study of individual galaxies which is beyond the scope of this paper.

8 CONCLUSIONS

We compared global properties of galaxies in the cosmological hydrodynamical simulation EAGLE and from two SA models of galaxy formation, L-GALAXIES and GALFORM. All the models in this comparison include physical prescriptions for the processes considered to be most important for galaxy formation, namely gas cooling, star formation, metal enrichment, feedback from stars and AGN, and, in the case of the SA models, environmental processes (which arise naturally in hydrodynamical simulations). For this comparison, all three models are produced from simulations from the same initial conditions, with the SA models built on merger trees constructed from the EAGLEDMO simulation (see Table 1). The simulations follow a cubic volume of side 100 comoving Mpc, with 1504^3 dark matter particles, and an equivalent number of baryonic particles for EAGLE, with cosmological parameters set by results from the *Planck* mission (Planck Collaboration XVI 2014, see also Table 2). Relative to the published models, only one significant change was implemented, in the case of GALFORM, a gradual ram-pressure stripping prescription for the hot gas in satellite galaxies replaced the instantaneous one. This change has the primary effect or reducing the fraction of satellite galaxies found to be passive. As a result of this change and the use of the merger trees from the EAGLEDMO, both SA models required a modest amount of recalibration to match the observational diagnostics at $z \approx 0$, summarized in Table 3. But note that no attempt was made to match the SA models to the EAGLE results.

This paper focuses on properties that encapsulate the evolution of typical galaxies with $M_* > 10^8\,\mathrm{M}_\odot$. In particular, we compare stellar masses, including the GSMF and its evolution, mean halo occupation, star formation properties, metallicities and galaxy sizes. By construction, the three GSMFs at $z = 0$ are in reasonable agreement, with differences below 0.5 dex for galaxies with $10^{8.0} < M_*/\mathrm{M}_\odot < 10^{11}$. Nevertheless, the evolution with redshift of the GSMF and other properties are not determined by the calibration of the model free parameters (which are set by observations at $z \approx 0$, as summarized in Table 3).

The GSMFs at $z \leq 2$ are in reasonable agreement for all three models, with differences in number density below 0.5 dex for galaxies with $10^{8.0} < M_*/\mathrm{M}_\odot < 10^{10.5}$ (Fig. 1). The stellar mass densities differ by $\lesssim$0.3 dex at $0 < z < 5$ (Fig. 3). At each redshift, star-forming galaxies have been defined using the same cut in sSFR for all the models (Section 2.3). At $z \leq 2$, the median sSFR in the three models agree within ≈0.4 dex for star-forming galaxies with $10^{8.0} < M_*/\mathrm{M}_\odot < 10^{9.5}$ (Fig. 7). For all three models, the median sSFR closely follows the mass assembly history of the host

dark matter halo (Fig. 9). These similarities indicate that the galaxy populations evolve in a consistent way across all models.

In spite of the overall good agreement, some discrepancies were uncovered, which can guide improvements to future models. These differences and their significance are summarized below.

(i) Despite the good agreement found for the global GSMFs, the GSMFs for central passive galaxies exhibit clear differences (Fig. 2). In both EAGLE and L-GALAXIES there is an excess of central passive galaxies with $M_* < 10^{9.5}\,\mathrm{M}_\odot$ that is not present in GALFORM. This excess is at least partly due to ejected satellite galaxies, i.e. galaxies that were once close to the centre of a larger halo, thus experiencing suppressed star formation due to environmental processes, such as ram-pressure stripping of hot gas, but that at later times are identified as central galaxies in their own haloes by some merger trees construction algorithms, such as those used in EAGLE and L-GALAXIES. In SA models, only the galaxies classified as central will be allowed to accrete new gas, which might lead to the formation of new stars, making a difference to their SF histories, with respect to galaxies classified as satellites.

(ii) Several differences suggest that in L-GALAXIES the AGN feedback is not as efficient in quenching star formation as in the other two models. This difference with respect to EAGLE and GALFORM drives L-GALAXIES to have a higher stellar mass density for star-forming galaxies with $M_* > 10^8\,\mathrm{M}_\odot$ at $z < 1.5$ (Fig. 3), a higher stellar mass–halo mass relation for haloes with $M_{\rm halo} \approx 10^{12}\,\mathrm{M}_\odot$ at $z = 0$ (Fig. 4), a higher normalization of the SFRD at $z < 1.5$ (Fig. 6) and a higher median sSFR for star-forming galaxies with $M_* > 10^{10.5}\,\mathrm{M}_\odot$ at all redshifts explored (Fig. 7). Note that the exact variations in normalization depend on the definition of star-forming galaxies. In order to decide which model has the most realistic modelling of the effect of feedback, a detailed comparison with observations is required, while simultaneously increasing the sample of simulated massive galaxies where AGN are found to have an impact by considering larger volumes. Similar comments are also relevant for establishing the level of realism of other modelled physical processes, such as the need for a threshold in gas density for star formation to happen.

(iii) In GALFORM there is a higher number of star-forming galaxies with $M_* < 10^{9.5}\,\mathrm{M}_\odot$ than in the other two models (Figs 2 and 8). This difference is related to GALFORM having a weaker stellar feedback or possibly a shorter reincorporation time-scale for the reheated gas in galaxies. A comprehensive study of this point will be done in a future paper following individual haloes.

(iv) Environmental processes are naturally accounted for in hydrodynamic simulations. The comparison between observations and variations of GALFORM with EAGLE has reinforced the need to model the stripping of the gas from satellite galaxies in a gradual manner and not instantaneously (Figs 2 and 8).

(v) The gas and stellar mass–metallicity relations and their evolution are very different among the three models, in particular for low-mass galaxies (see Figs 11 and 12). While the mass–metallicity relations do not evolve significantly in the two SA models, there is a clear flattening with time of the relation for EAGLE, which appears to be closer to observations (see Fig. 12). The lack of evolution for the two SA models is due to the metal mass following, on average, the growth of stellar mass, which is not the case in EAGLE. Note, however, that the mass–metallicity relations in the main EAGLE simulation are not converged at the low stellar mass end: higher resolution EAGLE simulations result in steeper mass–metallicity relations than those presented here (Schaye et al. 2015). In order to better understand the evolution of the mass–metallicity relations, higher resolution simulations are needed for EAGLE. In the case of the SA models, winds can be treated in a more realistic way, for example by using a dynamical model of SN feedback following the evolution of pressurized bubbles (Lagos et al. 2013). The treatment of winds has a direct impact on the evolution of galaxies hosted by small haloes. The justification of these changes will certainly require further detailed investigations of the chemical evolution of gas and stars in both hydrodynamical simulation, SA models, and observations.

(vi) The three models also predict different stellar mass–size relations (Fig. 13). The differences between the two SA models stem from different approaches to modelling the effect that the self-gravity of baryons has on both the baryons themselves and on their host dark matter haloes: while L-GALAXIES neglects these effects, GALFORM uses an approach that overpredicts them. The effect that baryons have on the underlying dark matter is naturally accounted for in EAGLE. One other aspect that affects the stellar mass–size relation is the simple assumptions made by the two SA models for modelling the evolution of the angular momentum. The scatter in the stellar mass–size relation is a factor of ≈2 larger in the two SA models compared to EAGLE. We have not found a satisfactory explanation for this difference. It is likely that this difference is related to the way the angular momentum of discs is tracked in the SA models. To explore this possibility further, it will be useful to follow galaxies hosted by the same halo in both EAGLE and the SA models.

There is a reasonable agreement between EAGLE and the SA models in many instances, which implies that the SA models are adequately encapsulating many of the physical processes relevant for this study that are naturally solved by hydrodynamical simulations. The level of agreement also shows that the subgrid physics prescriptions in the hydrodynamical simulation can now result in galaxy populations that have, at least, a similar level of realism as SA models. In some instances, an agreement between models could be due to a combination of interplaying model processes. Thus, although such similarities can help improve our understanding of the most likely physical process contributing to the evolution of a given galactic property in hydrodynamical simulation, a detailed comparison with observations is needed to advance towards more realistic models. Nevertheless, this comparison between models has highlighted how different modelling techniques can inform future developments by investigating the similarities and differences in the global model galaxy population. Further insights can for example be gained by using individual object comparisons, together with observational data.

ACKNOWLEDGEMENTS

We would like to thank Peder Norberg, James Trayford and Carlton Baugh for fruitful discussions. VGP acknowledges support from a European Research Council Starting Grant (DEGAS-259586). QiG acknowledges support from the NSFC grant (No. 11133003), the Strategic Priority Research Program The Emergence of Cosmological Structure of the Chinese Academy of Sciences (No. XDB09000000) and the 'Recruitment Program of Global Youth Experts' of China, the NAOC grant (Y434011V01). CPL is funded by an Australian Research Council Discovery Early Career Researcher Award (DE150100618). CSF acknowledges the ERC Advanced Investigation grant 'Cosmiway' (GA 267291). This work was supported by the Science and Technology Facilities Council (ST/L00075X/1); European Research Council (GA 267291 and

GA 259586) and by the Interuniversity Attraction Poles Programme initiated by the Belgian Science Policy Oce (AP P7/08 CHARM). This work used the DiRAC Data Centric system at Durham University, operated by the Institute for Computational Cosmology on behalf of the STFC DiRAC HPC Facility (www.dirac.ac.uk). This equipment was funded by BIS National E-infrastructure capital grant ST/K00042X/1, STFC capital grants ST/H008519/1 and ST/K00087X/1, STFC DiRAC Operations grant ST/K003267/1 and Durham University. DiRAC is part of the National E-Infrastructure. We acknowledge PRACE for awarding us access to the Curie machine based in France at TGCC, CEA, Bruyeres-le-Châtel. The data are available from the two lead authors.

REFERENCES

Allende Prieto C., Lambert D. L., Asplund M., 2001, ApJ, 556, L63
Asplund M., Grevesse N., Sauval A. J., Scott P., 2009, ARA&A, 47, 481
Bahé Y. M., McCarthy I. G., Balogh M. L., Font A. S., 2013, MNRAS, 430, 3017
Baldry I. K., Glazebrook K., Driver S. P., 2008, MNRAS, 388, 945
Baldry I. K. et al., 2012, MNRAS, 421, 621
Bauer A. E. et al., 2013, MNRAS, 434, 209
Baugh C. M., 2006, Rep. Prog. Phys., 69, 3101
Behroozi P. S., Wechsler R. H., Conroy C., 2013, ApJ, 770, 57
Benson A. J., 2010, Phys. Rep., 495, 33
Benson A. J., 2014, MNRAS, 444, 2599
Benson A. J., Bower R., 2011, MNRAS, 410, 2653
Benson A. J., Baugh C. M., Cole S., Frenk C. S., Lacey C. G., 2000, MNRAS, 316, 107
Benson A. J., Pearce F. R., Frenk C. S., Baugh C. M., Jenkins A., 2001, MNRAS, 320, 261
Bigiel F., Leroy A., Walter F., Brinks E., de Blok W. J. G., Madore B., Thornley M. D., 2008, AJ, 136, 2846
Blitz L., Rosolowsky E., 2006, ApJ, 650, 933
Blumenthal G. R., Faber S. M., Flores R., Primack J. R., 1986, ApJ, 301, 27
Booth C. M., Schaye J., 2009, MNRAS, 398, 53
Boselli A., Cortese L., Boquien M., Boissier S., Catinella B., Gavazzi G., Lagos C., Saintonge A., 2014, A&A, 564, A67
Bower R. G., Benson A. J., Malbon R., Helly J. C., Frenk C. S., Baugh C. M., Cole S., Lacey C. G., 2006, MNRAS, 370, 645
Bower R. G., Vernon I., Goldstein M., Benson A. J., Lacey C. G., Baugh C. M., Cole S., Frenk C. S., 2010, MNRAS, 407, 2017
Bower R. G., Benson A. J., Crain R. A., 2012, MNRAS, 422, 2816
Boylan-Kolchin M., Springel V., White S. D. M., Jenkins A., Lemson G., 2009, MNRAS, 398, 1150
Bruzual A. G., Charlot S., 1993, ApJ, 405, 538
Bruzual G., Charlot S., 2003, MNRAS, 344, 1000
Burgarella D. et al., 2013, A&A, 554, A70
Cattaneo A. et al., 2007, MNRAS, 377, 63
Chabrier G., 2003, PASP, 115, 763
Cole S., Lacey C. G., Baugh C. M., Frenk C. S., 2000, MNRAS, 319, 168
Cole S. et al., 2001, MNRAS, 326, 255
Conroy C., White M., Gunn J. E., 2010, ApJ, 708, 58
Contreras S., Baugh C. M., Norberg P., Padilla N., 2013, MNRAS, 432, 2717
Correa C. A., Wyithe J. S. B., Schaye J., Duffy A. R., 2015, MNRAS, 450, 1514
Cowie L. L., Binney J., 1977, ApJ, 215, 723
Crain R. A. et al., 2015, MNRAS, 450, 1937
Croton D. J. et al., 2006, MNRAS, 365, 11
Cucciati O. et al., 2012, A&A, 539, A31
Dalla Vecchia C., Schaye J., 2012, MNRAS, 426, 140
Davis M., Efstathiou G., Frenk C. S., White S. D. M., 1985, ApJ, 292, 371
De Lucia G., Blaizot J., 2007, MNRAS, 375, 2
De Lucia G., Boylan-Kolchin M., Benson A. J., Fontanot F., Monaco P., 2010, MNRAS, 406, 1533
De Lucia G., Tornatore L., Frenk C. S., Helmi A., Navarro J. F., White S. D. M., 2014, MNRAS, 445, 970
Dekel A. et al., 2009, Nature, 457, 451
Dolag K., Borgani S., Murante G., Springel V., 2009, MNRAS, 399, 497
Driver S. P. et al., 2012, MNRAS, 427, 3244
Dubois Y. et al., 2014, MNRAS, 444, 1453
Fakhouri O., Ma C.-P., Boylan-Kolchin M., 2010, MNRAS, 406, 2267
Fanidakis N., Baugh C. M., Benson A. J., Bower R. G., Cole S., Done C., Frenk C. S., 2011, MNRAS, 410, 53
Favole G. et al., 2015, preprint (arXiv:1507.04356)
Font A. S. et al., 2008, MNRAS, 389, 1619
Fontanot F., Pasquali A., De Lucia G., van den Bosch F. C., Somerville R. S., Kang X., 2011, MNRAS, 413, 957
Franx M., van Dokkum P. G., Förster Schreiber N. M., Wuyts S., Labbé I., Toft S., 2008, ApJ, 688, 770
Fumagalli M., Fossati M., Hau G. K. T., Gavazzi G., Bower R., Sun M., Boselli A., 2014, MNRAS, 445, 4335
Furlong M. et al., 2015a, preprint (arXiv:1510.05645)
Furlong M. et al., 2015b, MNRAS, 450, 4486
Gao L., Loeb A., Peebles P. J. E., White S. D. M., Jenkins A., 2004, ApJ, 614, 17
Genel S. et al., 2008, ApJ, 688, 789
Genel S. et al., 2012, ApJ, 745, 11
Gilbank D. G., Baldry I. K., Balogh M. L., Glazebrook K., Bower R. G., 2010, MNRAS, 405, 2594
Gilbank D. G. et al., 2011, MNRAS, 414, 304
Gnedin O. Y., Kravtsov A. V., Klypin A. A., Nagai D., 2004, ApJ, 616, 16
Gonzalez-Perez V., Baugh C. M., Lacey C. G., Kim J.-W., 2011, MNRAS, 417, 517
Gonzalez-Perez V., Lacey C. G., Baugh C. M., Lagos C. D. P., Helly J., Campbell D. J. R., Mitchell P. D., 2014, MNRAS, 439, 264
Granato G. L., Lacey C. G., Silva L., Bressan A., Baugh C. M., Cole S., Frenk C. S., 2000, ApJ, 542, 710
Gunawardhana M. L. P. et al., 2015, MNRAS, 447, 875
Guo Q., White S. D. M., 2008, MNRAS, 384, 2
Guo Q. et al., 2011, MNRAS, 413, 101
Guo Q. et al., 2013, MNRAS, 435, 897
Haardt F., Madau P., 2001, in Neumann D. M., Tran J. T. V., eds, Clusters of Galaxies and the High Redshift Universe Observed in X-rays. CEA, Saclay, p. 64
Hahn O., Carollo C. M., Porciani C., Dekel A., 2007, MNRAS, 381, 41
Häring N., Rix H.-W., 2004, ApJ, 604, L89
Helly J. C., Cole S., Frenk C. S., Baugh C. M., Benson A., Lacey C., Pearce F. R., 2003, MNRAS, 338, 913
Henriques B. M. B., Thomas P. A., Oliver S., Roseboom I., 2009, MNRAS, 396, 535
Henriques B. M. B., White S. D. M., Thomas P. A., Angulo R., Guo Q., Lemson G., Springel V., Overzier R., 2015, MNRAS, 451, 2663
Hirschmann M., Naab T., Somerville R. S., Burkert A., Oser L., 2012, MNRAS, 419, 3200
Hirschmann M., Dolag K., Saro A., Bachmann L., Borgani S., Burkert A., 2014a, MNRAS, 442, 2304
Hirschmann M., De Lucia G., Wilman D., Weinmann S., Iovino A., Cucciati O., Zibetti S., Villalobos Á., 2014b, MNRAS, 444, 2938
Hirschmann M., De Lucia G., Fontanot F., 2016, MNRAS, 461, 1760
Hoffman Y., Metuki O., Yepes G., Gottlöber S., Forero-Romero J. E., Libeskind N. I., Knebe A., 2012, MNRAS, 425, 2049
Hopkins P. F., Kereš D., Oñorbe J., Faucher-Giguère C.-A., Quataert E., Murray N., Bullock J. S., 2014, MNRAS, 445, 581
Ilbert O. et al., 2013, A&A, 556, A55
Jenkins A., 2010, MNRAS, 403, 1859
Jiang L., Helly J. C., Cole S., Frenk C. S., 2014, MNRAS, 440, 2115
Karim A. et al., 2011, ApJ, 730, 61
Katz N., 1992, ApJ, 391, 502
Kauffmann G., 1996, MNRAS, 281, 487
Kennicutt R. C., Jr, 1983, ApJ, 272, 54
Kennicutt R. C., Jr, 1998, ApJ, 498, 541

Khandai N., Di Matteo T., Croft R., Wilkins S., Feng Y., Tucker E., DeGraf C., Liu M.-S., 2015, MNRAS, 450, 1349
Knebe A. et al., 2015, MNRAS, 451, 4029
Lacey C., Cole S., 1993, MNRAS, 262, 627
Lacey C. G. et al., 2015, preprint (arXiv:1509.08473)
Lagos C. D. P., Lacey C. G., Baugh C. M., Bower R. G., Benson A. J., 2011, MNRAS, 416, 1566
Lagos C. d. P., Lacey C. G., Baugh C. M., 2013, MNRAS, 436, 1787
Lagos C. d. P., Davis T. A., Lacey C. G., Zwaan M. A., Baugh C. M., Gonzalez-Perez V., Padilla N. D., 2014, MNRAS, 443, 1002
Lagos C. d. P., Padilla N. D., Davis T. A., Lacey C. G., Baugh C. M., Gonzalez-Perez V., Zwaan M. A., Contreras S., 2015a, MNRAS, 448, 1271
Lagos C. d. P. et al., 2015b, MNRAS, 452, 3815
Lee J. et al., 2014, MNRAS, 445, 4197
Leroy A. K., Walter F., Brinks E., Bigiel F., de Blok W. J. G., Madore B., Thornley M. D., 2008, AJ, 136, 2782
Li C., White S. D. M., 2009, MNRAS, 398, 2177
Li R., Gao L., Xie L., Guo Q., 2013, MNRAS, 435, 3592
Libeskind N. I., Hoffman Y., Knebe A., Steinmetz M., Gottlöber S., Metuki O., Yepes G., 2012, MNRAS, 421, L137
Lu Y., Kereš D., Katz N., Mo H. J., Fardal M., Weinberg M. D., 2011a, MNRAS, 416, 660
Lu Y., Mo H. J., Weinberg M. D., Katz N., 2011b, MNRAS, 416, 1949
Lu Y. et al., 2014, ApJ, 795, 123
Ma X., Hopkins P. F., Faucher-Giguere C.-A., Zolman N., Muratov A. L., Keres D., Quataert E., 2016, MNRAS, 456, 2140
McAlpine S. et al., 2016, Astron. Comput., 15, 72
McCarthy I. G., Frenk C. S., Font A. S., Lacey C. G., Bower R. G., Mitchell N. L., Balogh M. L., Theuns T., 2008, MNRAS, 383, 593
McConnell N. J., Ma C.-P., 2013, ApJ, 764, 184
McGee S. L., Bower R. G., Balogh M. L., 2014, MNRAS, 442, L105
Marigo P., 2001, A&A, 370, 194
Marinacci F., Pakmor R., Springel V., 2014, MNRAS, 437, 1750
Mitchell P. D., Lacey C. G., Cole S., Baugh C. M., 2014, MNRAS, 444, 2637
Mitchell P., Lacey C., Baugh C., Cole S., 2016, MNRAS, 456, 1459
Monaco P., Benson A. J., De Lucia G., Fontanot F., Borgani S., Boylan-Kolchin M., 2014, MNRAS, 441, 2058
Moustakas J. et al., 2013, ApJ, 767, 50
Muzzin A. et al., 2013, ApJ, 777, 18
Navarro J. F., White S. D. M., 1993, MNRAS, 265, 271
Neistein E., van den Bosch F. C., Dekel A., 2006, MNRAS, 372, 933
Neistein E., Khochfar S., Dalla Vecchia C., Schaye J., 2012, MNRAS, 421, 3579
Newman A. B., Ellis R. S., Treu T., 2015, ApJ, 814, 26
Norberg P. et al., 2002, MNRAS, 336, 907
Okamoto T., Shimizu I., Yoshida N., 2014, PASJ, 66, 70
Oppenheimer B. D., Davé R., Kereš D., Fardal M., Katz N., Kollmeier J. A., Weinberg D. H., 2010, MNRAS, 406, 2325
Parkinson H., Cole S., Helly J., 2008, MNRAS, 383, 557
Peebles P. J. E., 1980, The Large-scale Structure of the Universe. Princeton Univ. Press, Princeton, NJ
Planck Collaboration XVI, 2014, A&A, 571, A16
Portinari L., Chiosi C., Bressan A., 1998, A&A, 334, 505
Puchwein E., Springel V., 2013, MNRAS, 428, 2966
Rodighiero G. et al., 2010, A&A, 518, L25
Rosas-Guevara Y. M. et al., 2015, MNRAS, 454, 1038
Ruiz A. N. et al., 2015, ApJ, 801, 139
Saro A., De Lucia G., Borgani S., Dolag K., 2010, MNRAS, 406, 729
Sawala T., Frenk C. S., Crain R. A., Jenkins A., Schaye J., Theuns T., Zavala J., 2013, MNRAS, 431, 1366
Schaller M. et al., 2015a, MNRAS, 451, 1247
Schaller M., Dalla Vecchia C., Schaye J., Bower R. G., Theuns T., Crain R. A., Furlong M., McCarthy I. G., 2015b, MNRAS, 454, 2277
Schaye J., 2004, ApJ, 609, 667
Schaye J., Dalla Vecchia C., 2008, MNRAS, 383, 1210
Schaye J. et al., 2015, MNRAS, 446, 521
Schechter P., 1976, ApJ, 203, 297
Scott T. C., Usero A., Brinks E., Boselli A., Cortese L., Bravo-Alfaro H., 2013, MNRAS, 429, 221
Segers M. C., Crain R. A., Schaye J., Bower R. G., Furlong M., Schaller M., Theuns T., 2016, MNRAS, 456, 1235
Shen S., Mo H. J., White S. D. M., Blanton M. R., Kauffmann G., Voges W., Brinkmann J., Csabai I., 2003, MNRAS, 343, 978
Silk J., 1977, ApJ, 211, 638
Silverman B. W., 1986, Density Estimation for Statistics and Data Analysis. Chapman and Hall, London
Somerville R. S., Davé R., 2015, ARA&A, 53, 51
Sousbie T., 2011, MNRAS, 414, 350
Springel V., 2005, MNRAS, 364, 1105
Springel V., White S. D. M., Tormen G., Kauffmann G., 2001, MNRAS, 328, 726
Steinborn L. K., Dolag K., Hirschmann M., Prieto M. A., Remus R.-S., 2015, MNRAS, 448, 1504
Stringer M. J., Brooks A. M., Benson A. J., Governato F., 2010, MNRAS, 407, 632
Tempel E., Saar E., Liivamägi L. J., Tamm A., Einasto J., Einasto M., Müller V., 2011, A&A, 529, A53
Thielemann F.-K. et al., 2003, in Hillebrandt W., Leibundgut B., eds, From Twilight to Highlight: The Physics of Supernovae. Springer-Verlag, Heidelberg, p. 331
Trayford J. W. et al., 2015, MNRAS, 452, 2879
Tremonti C. A. et al., 2004, ApJ, 613, 898
van de Voort F., Schaye J., 2012, MNRAS, 423, 2991
Velliscig M., van Daalen M. P., Schaye J., McCarthy I. G., Cacciato M., Le Brun A. M. C., Dalla Vecchia C., 2014, MNRAS, 442, 2641
Vogelsberger M. et al., 2014, MNRAS, 444, 1518
Wechsler R. H., Bullock J. S., Primack J. R., Kravtsov A. V., Dekel A., 2002, ApJ, 568, 52
Weinmann S. M., Pasquali A., Oppenheimer B. D., Finlator K., Mendel J. T., Crain R. A., Macciò A. V., 2012, MNRAS, 426, 2797
Wetzel A. R., Tinker J. L., Conroy C., van den Bosch F. C., 2014, MNRAS, 439, 2687
White S. D. M., Frenk C. S., 1991, ApJ, 379, 52
White S. D. M., Rees M. J., 1978, MNRAS, 183, 341
Wiersma R. P. C., Schaye J., Smith B. D., 2009a, MNRAS, 393, 99
Wiersma R. P. C., Schaye J., Theuns T., Dalla Vecchia C., Tornatore L., 2009b, MNRAS, 399, 574
Yates R. M., Henriques B., Thomas P. A., Kauffmann G., Johansson J., White S. D. M., 2013, MNRAS, 435, 3500
Yoshida N., Stoehr F., Springel V., White S. D. M., 2002, MNRAS, 335, 762
Zahid H. J., Geller M. J., Kewley L. J., Hwang H. S., Fabricant D. G., Kurtz M. J., 2013, ApJ, 771, L19
Zahid H. J., Dima G. I., Kudritzki R.-P., Kewley L. J., Geller M. J., Hwang H. S., Silverman J. D., Kashino D., 2014, ApJ, 791, 130
Zehavi I. et al., 2011, ApJ, 736, 59
Zolotov A. et al., 2012, ApJ, 761, 71

APPENDIX A: HALO MASSES

Haloes in both the EAGLE simulation and the L-GALAXIES model are identified by combining the FoF (Davis et al. 1985) algorithm with the SUBFIND code (Springel et al. 2001; Dolag et al. 2009). In both cases, a sphere centred at the minimum of the gravitational potential of each halo is grown until the mass contained within a given radius, R_{200}, reaches $M_{200}^{\rm crit} = 200\left(4\pi\rho_{\rm crit}(z)R_{200}^3/3\right)$, where $\rho_{\rm crit}(z) = 3H(z)^2/8\pi G$ is the critical density at the redshift of interest. The GALFORM model, although initially it also uses the FoF haloes and their internal self-bound substructures as identified by SUBFIND, actually identifies haloes, the Dhaloes, taking into account the merger tree construction process (Jiang et al. 2014, see also Section 2.2.1). The mass of a Dhalo is simply the sum of the masses

of its component subhaloes (note that no particle can belong to more than one Dhalo). These, by construction, are different from those found initially in some of the FoF groups. In order to compare the host halo masses of galaxies predicted by the three considered models, we have estimated the $M_{200}^{\rm crit}$ for the identified Dhaloes used by GALFORM. This is done by using the centres of the Dhaloes and calculating the mass enclosed in a sphere around this centre with a mean overdensity equal to 200 times the critical value, i.e. using the same definition for $M_{200}^{\rm crit}$ as in EAGLE and L-GALAXIES. Although this definition is similar, the centres of the Dhaloes and those haloes identified with the FoF algorithm can be different, which will give rise to different halo masses in some cases. Throughout this paper we simply refer to the $M_{200}^{\rm crit}$ obtained as described above as $M_{\rm halo}$.

In GALFORM, the reconstructed $M_{200}^{\rm crit}$ can be bigger than the original Dhalo mass by up to a factor of 4 for haloes hosting small galaxies with stellar masses below 10^8 M$_\odot$. This happens because the R_{200} of these small haloes actually encloses mass from their neighbouring haloes, which will be counted towards their $M_{200}^{\rm crit}$. Thus, no galaxy with stellar mass below 10^8 M$_\odot$ will be considered in the comparison. Note that, in any case, 10^8 M$_\odot$ is below the resolution limit of the largest EAGLE simulation.

Here, we comment on the variations obtained when the native Dhalo mass is used for GALFORM haloes. For galaxies with stellar masses above 10^8 M$_\odot$ at $z = 0$, an average shift of 0.07 dex is found between the stellar mass–halo mass relation (see Section 3.3) for GALFORM haloes when using either $M_{200}^{\rm crit}$ or the native Dhalo masses, with $M_{200}^{\rm crit}$ being larger at $z = 0$, when the differences are the largest. A maximum shift of 0.13 dex is found at $z = 0$. The differences are smaller at higher redshifts. Similar results to those discussed in Section 3.3.1, are found for the $\langle N \rangle_M$ obtained utilizing the Dhalo mass for GALFORM haloes instead of $M_{200}^{\rm crit}$. The same is true for the probability density distribution of satellite galaxies separated according to the mass of their host halo, discussed in Section 5.4.1.

A1 The halo mass function

Fig. A1 shows the halo mass function constructed from the $M_{200}^{\rm crit}$ of the host haloes of central galaxies in EAGLE, GALFORM and L-GALAXIES. At $z = 0$, the three models predict halo mass functions which are in very good agreement above 10^{12} M$_\odot$, although, beyond 10^{14} M$_\odot$ the results are not statistically significant due to the small numbers of very massive haloes within the EAGLEDMO simulation. This trend remains true at higher redshifts.

Fig. A1 shows that the halo mass functions for the two SA models are remarkably similar, with differences ranging from about 5 to 15 per cent, depending on the halo mass. This difference is likely caused by the different definitions of central galaxies in the two SA models.

The halo mass functions predicted by both SA models are above that from EAGLE for haloes below $\approx 10^{13.5}$, $\approx 10^{13}$ and $\approx 10^{12}$ M$_\odot$ at $z = 0, 1$ and 2, respectively. At $z = 0$, the halo mass function derived from GALFORM is actually above that from EAGLE for all the explored halo masses. Several authors have previously found that the early loss of baryons due to stellar feedback can reduce the growth rate of those dark matter haloes that have masses below 10^{13} M$_\odot$ at $z = 0$ (e.g. Sawala et al. 2013). Schaller et al. (2015a) found that, in the EAGLE simulation, the reduction in halo mass also happens for haloes hosting galaxies affected by AGN feedback, and that this change is milder than for those dominated by stellar feedback.

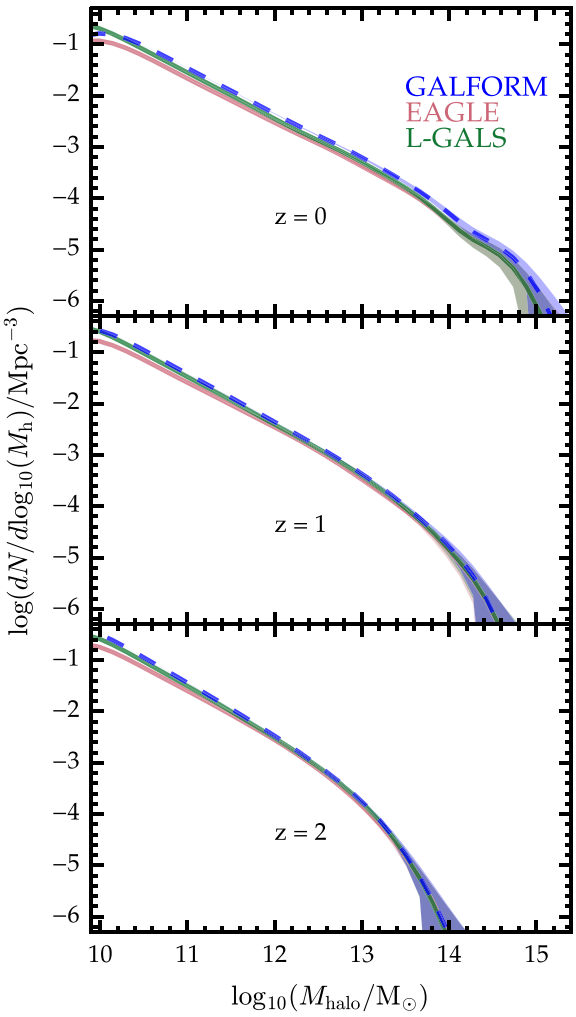

Figure A1. The halo mass function constructed from the $M_{200}^{\rm crit}$ of the host haloes of all central galaxies in EAGLE (red lines), GALFORM (blue dashed lines) and L-GALAXIES (green lines) at $z = 0$, 1 and 2 from top to bottom. The shaded regions show the 1σ range obtained by bootstrapping 200 realizations of the halo mass function. Although the three models are in remarkably good agreement at the massive end, the mass functions from the two SA models are clearly above that for EAGLE for haloes with $\lesssim 10^{11.5}$ M$_\odot$ due to the early loss of baryons by feedback in EAGLE.

APPENDIX B: CALIBRATION OF THE SA MODELS

In this work we make use of two SA models, L-GALAXIES and GALFORM, based upon the published versions described in Guo et al. (2013) and Gonzalez-Perez et al. (2014), respectively. As described in detail in Section 2, the two SA models have been run using merger trees from the EAGLEDMO simulation, which assumes a different cosmology and has a higher mass resolution than the underlying simulation used in these published models. Moreover, the merger trees from the EAGLEDMO simulation were constructed based on 200 snapshots, while those used by Guo et al. (2013) and Gonzalez-Perez et al. (2014) were based on only 64. Although the time resolution can affect the implementation of SA models, our tests with these two flavours of L-GALAXIES and GALFORM, showed the impact to be minimal for the global properties studied here. In order to reduce the initial differences between EAGLE, L-GALAXIES and GALFORM, the same Chabrier IMF (Chabrier 2003) was adopted in

Table B1. Modifications, besides the cosmology, to the GALFORM model used in this work with respect to the published model described in Gonzalez-Perez et al. (2014). Note that $\alpha_{\rm cool}$ is one of the parameters setting the AGN feedback efficiency in GALFORM (Lacey et al. 2015).

Parameter	Gonzalez-Perez et al. (2014)	This Work
IMF	Kennicutt	Chabrier
Yield	0.021	0.02908
Recycle fraction	0.44	0.4588
SPS model	BC99	CW10
Stripping of hot gas	Instantaneous	Gradual
$\alpha_{\rm cool}$ (AGN feedback)	0.60	0.52

Table B2. Modifications, besides the cosmology, to the L-GALAXIES model used in this work with respect to the published model described in Guo et al. (2013). In the Guo et al. (2013) model, the parameters k and ϵ are related to the galaxy feedback, as stated in the table.

Parameter	Guo et al. (2013)	This Work
Yield	0.03	0.029 08
Recycle fraction	0.43	0.4588
AGN efficiency, $k(10^{-5}\,{\rm M}_{\odot})$	0.7	3
Threshold mass of cold gas reheated due to star formation, ϵ	4.0	4.5

GALFORM, with the consequent modification in the metal yield and recycled fractions. The choice of SPS model was changed from BC99 (an update of Bruzual A. & Charlot 1993) to that from Conroy et al. (2010, CW10), which is closer to the SPS from Bruzual & Charlot (2003) assumed in both EAGLE and L-GALAXIES. This change of SPS results in negligible differences in all the studied properties. In order for the passive fractions at $z = 0$ from the three studied models to give a reasonable match to observations, one additional change was included in the GALFORM model: a gradual ram-pressure stripping of the hot gas in satellite galaxies. These changes, together with the change in cosmology and mass resolution of the underlying simulation, resulted in model luminosity functions and GSMFs at $z = 0$ that do not agree as well with observations as the published models (see Section 2.2.3 for more details). Thus, a small adjustment of the model parameters controlling the feedback was made. The changes with respect to the published models are summarized in Tables B2 and B1.

L-GALAXIES was calibrated using the GSMF at $z = 0$, among other properties (see Section 2.2.3 for more details). The changes in the parameters detailed in Table B2 result in a different GSMF, as shown in Fig. B2. This figure suggests that the SN and AGN feedback are more efficient in the model used for this work, compared with the published model in Guo et al. (2013).

The observed b_J- and K-band luminosity functions at $z = 0$ are shown in Fig. B1 together with those from the GALFORM model used for this study both with and instantaneous and a gradual ram-pressure stripping. These are the main observations used to calibrate the GALFORM models (see Section 2.2.3 for further details).

Figs B1 and B2 compare the published models, based on merger trees from the MS-W7 simulation (short dashed lines), with exactly

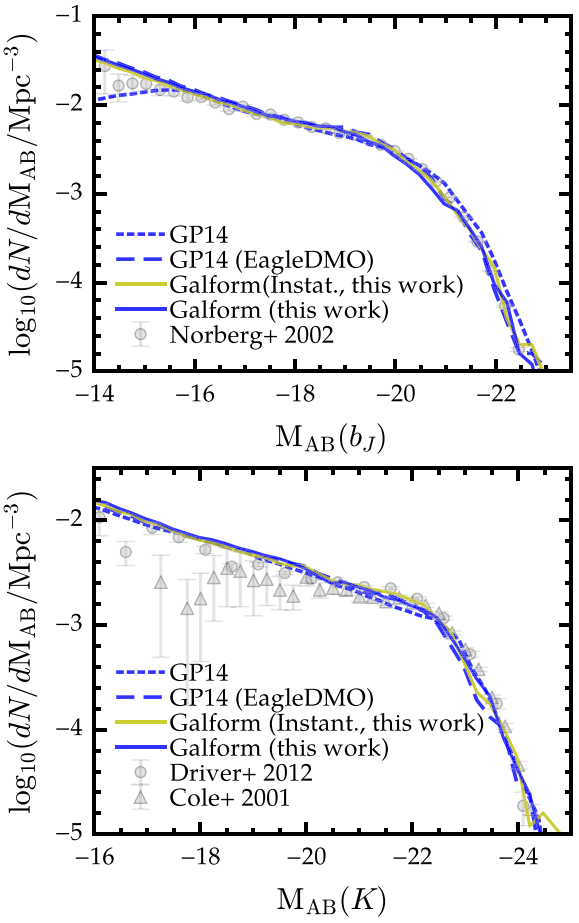

Figure B1. The predicted luminosity functions at redshift $z = 0$, in the b_J-band (top panel) and in the K-band (bottom panel) which are used by the GALFORM model in the calibration against the observations. The blue dashed lines are the predictions in Gonzalez-Perez et al. (2014). The dashed lines are the predictions of GP14 model based on EAGLEDMO. The yellow solid lines and blue solid lines are the predictions of the re-calibrated GALFORM model with instant and gradual ram-pressuring stripping in this work, respectively. The observational b_J- and K-band luminosity functions are plotted as grey points (Norberg et al. 2002) in top panel and grey triangles (Cole et al. 2001), grey points (Driver et al. 2012) in bottom panel, respectively.

the same models but run on the EAGLEDMO simulation merger trees (long dashed lines). The change in the mass resolution, from the MS-W7 to the EAGLEDMO simulation, is clear from comparing the two pairs of lines at small masses or luminosities. When the mass resolution is increased in the simulations, more model galaxies with smaller masses or fainter magnitudes are found. This comparison also shows that the combination of the change of cosmology together with the change of mass resolution is model dependent. A detailed study of this point, although interesting, is beyond the scope of this paper.

Figs B1 and B2 clearly show that the changes introduced in the SA models result in very small variations of the global properties used for their calibration, at least in the range where there is a large enough number of galaxies within the EAGLEDMO simulation, as to be statistically meaningful.

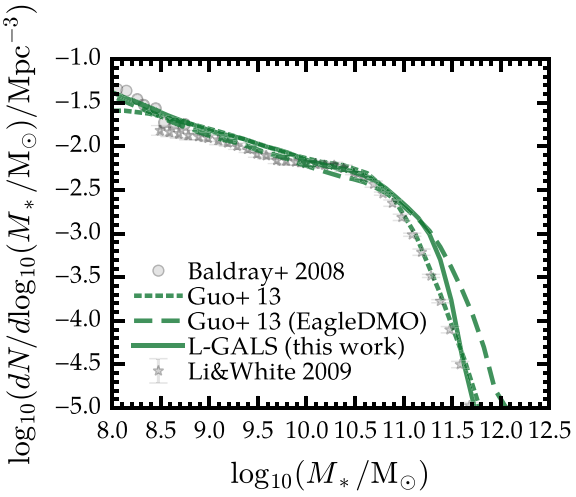

Figure B2. The predicted GSMF at redshift $z = 0$ which are used by the L-GALAXIES model in the calibration against the observations. The green dotted line is the prediction by Guo et al. (2013). The green dashed line is the predictions by L-GALAXIES model with the parameters are the same as in Guo et al. (2013) but based on EAGLEDMO. The green solid line is the predictions of re-calibrated L-GALAXIES model used in this work. The observations used in the calibration are plotted as grey points (Baldry et al. 2008) and grey stars (Li & White 2009).

This paper has been typeset from a TEX/LATEX file prepared by the author.